magnetochemistry

MDPI

Review

Hervé- and Krebs-Type Magnetic Polyoxometalate Dimers

Aleksandar Kondinski [1,*], Abhishek Banerjee [2,*] and Sib Sankar Mal [3,*]

[1] Department of Chemical Engineering and Biotechnology, University of Cambridge, Cambridge CB3 0AS, UK
[2] Department of Chemistry, Visvesvaraya National Institute of Technology (VNIT), Nagpur 440010, India
[3] Department of Chemistry, National Institute of Technology Karnataka (NITK), Surathkal, Mangalore 575 025, India
* Correspondence: aleksandar@kondinski.com (A.K.); abhishekbanerjee@chm.vnit.ac.in (A.B.); malss@nitk.edu.in (S.S.M.)

Abstract: Lacunary polyoxometalates (POMs) are negatively charged metal–oxo clusters, formally obtained from plenary topologies via fragment removal. Owing to the fragment removal, the lacunary POMs archetypes are rich in nucleophilic terminal oxo ligands, making them suitable for post-synthetic coordination with various heterometals. Trilacunary heteropolytungstates (hetero-POTs) based on bowl-shaped $\{W_9O_{30}\}$ framework incorporating a central lone-pair containing $\{XO_3\}$ hetergroup (X = As^{III}, Sb^{III}, and Bi^{III}) function as all-inorganic scaffolds that in the presence of d-block metal cations typically construct sandwich-like dimers of Hervé and/or Krebs. Herein we review the preparative approaches, as well as compositional and magnetic versatility of the constructed Hervé- and Krebs-type dimers and discuss prospective uses as POMtronics.

Keywords: polyoxometalates; dimers; polyoxotungstates; magnetism; synthesis; POMtronics

Citation: Kondinski, A.; Banerjee, A.; Mal, S.S. Hervé- and Krebs-Type Magnetic Polyoxometalate Dimers. *Magnetochemistry* **2022**, *8*, 96. https://doi.org/10.3390/magnetochemistry8090096

Academic Editor: Junwei Zhao

Received: 28 June 2022
Accepted: 21 August 2022
Published: 27 August 2022

1. Introduction

The structural and chemical versatility of molecular assemblies allowing fine-tuning of the magneto chemical phenomena has been a driving force for the development of many magnetic chemicals at the nanoscale [1]. Magnetic molecules show the potential for quantum bit (i.e., "qubit") information storage as a superposition of states, which opens an emerging application in quantum computing [2–7]. Considering existing challenges such as loss of quantum coherence, practical deployment is currently out of reach [8]; however, at the same time, the field shows many encouraging examples [9–14].

Polyoxometalates (POMs) represent a class of molecular metal oxides, typically comprised of early transition metals in high oxidation state(s) (mainly V, Mo, and W) [15,16]. POMs are one of the most complex of all-inorganic architectures [17], with broad applications in catalysis [18], materials science [19,20], and nanoelectronics [21,22]. Owing to their all-inorganic nature, high symmetry, and structural robustness, POMs have also been of high interest in molecular magnetism [23]. Plenary POMs exposing oxo-based cavities are typically used as scaffolds capable of stabilizing magnetic heterometallic cations, occasionally leading to single-ion magnets (SIMs) with spin qubit behavior [24,25]. Prominent examples are the lanthanide functionalized Preyssler POMs [23], and the cuboidal and pentagonal prismatic polyoxopalladates [21,26]. Some high symmetry, but partially or fully-reduced POMs, such as the semimetal-functionalized polyoxovanadates [27], mixed-metal Keplerates [28], are known to exhibit complex magneto-chemical behavior as well [29]. POMs with large internal cavities can exhibit multiple accessible oxo sites, successfully mimicking naturally occurring zeolites in incorporating multimetal magnetic nuclei [30], or even full metal–oxo clusters [31,32].

Low symmetry POMs derived by formal removal of metal–oxo fragments from the plenary POM archetypes are another form of synthetic scaffolds that can function as inorganic polydentate ligands [33,34]. These types of POMs can coordinate to various transition-metals, especially 3d [35], or rare-earth 4f-block metals [36], or a combination of 3d/4f magnetically active metal centers [37].

Owing to the good inertness of the W–O bonds, polyoxotungstates (POTs) exhibit the most studied class of lacunary POMs [38]. Most of the lacunary POTs are derived from the Kegginoidal archetype [39]. The Keggin type archetype is often viewed as a clathrate, where an $\{XO_4\}$ guest unit is encapsulated within an otherwise highly symmetrical and neutral $\{W_{12}O_{36}\}$ [39]. These shells can be of O_h or D_{3h} symmetry, assigned respectively as α- and β-Kegginoids (Figure 1). The formal removal of one $[WO]^{4+}$ unit leads to so-called monovacant or monolacunary POMs, which depending on the shell of derivation, can be further assigned as α, and β_{1-3} [40]. The formal removal of two or more metal centers leads to a complex configuration isomer problem considering many possibilities where the formal removal can occur [41,42]. However, the trilacunary Kegginoids derived by a formal removal of the $\{W_3O_6\}$ moiety, from the α-/β-$\{W_{12}O_{36}\}$, are most studied. The formed $\{W_9O_{30}\}$ bowl-like (C_{3v}) metal oxo shells are inherently isomeric and can incorporate tetrahedral $\{XO_4\}$ or lone-pair containing trigonal pyramidal $\{XO_3\}$ units. In the case of $\{XO_4\}$, the guest unit can point with one terminal oxo towards the bottom of the bowl (configuration A) or towards the exterior (i.e., opening) of the $\{W_9O_{30}\}$ bowl (configuration B). Configuration B is commonly observed among lone pair units containing $\{XO_3\}$, where X = As^{III}, Sb^{III} and Bi^{III}. Other lone pair units such as $\{S^{IV}O_3\}$ or $\{Se^{IV}O_3\}$ have also been observed to be incorporated within the cavity. The formed POMs can dimerize to form $[(XO_3)_2(WO_3)_{18}]^{n-}$ Wells–Dawson Type POMs [40,43].

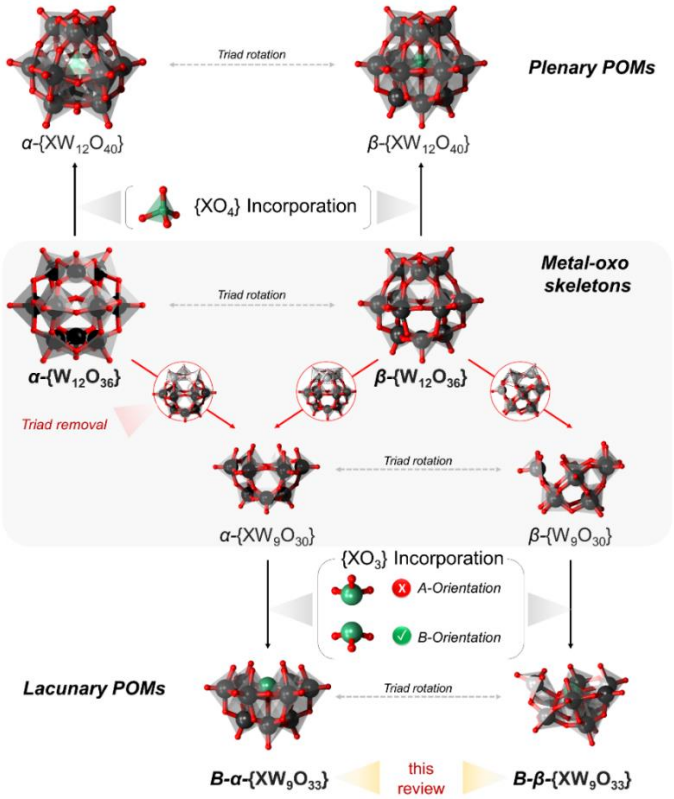

Figure 1. Concept map representation of the relationship between different metal–oxo skeletons (**middle row**) and the incorporation of tetrahedral guests $\{XO_4\}$ leading to complete plenary POMs (**top row**) or $\{XO_3\}$ guests leading to different lone pair containing lacunary POMs (**bottom row**). Color code: W = black, O = red X = green.

The trilacunary $[XW_9O_{33}]^{9-}$ ligands readily form by the condensation reaction of acidified aqueous mixtures of X_2O_3 (X = As^{III}, Sb^{III} and Bi^{III}.) and $Na_2WO_4{\cdot}2H_2O$ from an initial *pH* in the range between 7–9 [44–46]. These POMs represent one of the most utilized all-inorganic ligands for the preparation of heterometallic structures, occasionally agglomerating several hundred or even thousands of atoms [47]. However, among the most prominent structures produced by the $[XW_9O_{33}]^{9-}$ ligands are the Hervé- [48] and Krebs-type dimeric structures [46]. The lone pair-containing $[XW_9O_{33}]^{9-}$ POMs have different reactivity in contrast to their related non-lone-pair containing $[XW_9O_{34}]^{n-}$ types, that adopt $\{XO_4\}$ units with X = P^V, Si^{IV}, As^V, and Ge^{IV} [49]. The $\{XO_4\}$ heterogroup in $[XW_9O_{34}]^{n-}$ may adopt two different configurations [50], facilitating the formation of so-called Weakley [51], and Knoth-type dimer structures [52].

In this regard, the present review article focuses on sandwich-type complexes based on the trilacunary $[XW_9O_{33}]^{9-}$ and their post-synthetic derivatization. In the first line, we review the electronic, structural, and reactivity properties of these lacunary $[XW_9O_{33}]^{9-}$ POMs and discuss some general trends among them. Next, we systematically survey the reported Hervé- and Krebs-type assemblies and their magnetic properties. We have given here the inter-atomic coupling constants whenever reported by the authors, with the following convention $H = -JS_AS_B$.

2. Sandwich-Type POM Archetypes

α-$[XW_9O_{33}]^{9-}$ (X = As^{III}, Sb^{III}, and Bi^{III}) species exhibit six terminal oxo sites that are highly basic and able to coordinate to different hetero-metal centers. The oxo sites form a virtual distorted hexagonal plane normal to the 3-fold symmetric axis of rotation. The distortion can be traced to the arrangement of the central $\{XO_3\}$ unit, which shares its three oxo ligands with three pairs of tungsten centers, respectively. In this regard, the interatomic distances between terminal oxo centers that derive from a pair of edge-sharing $\{WO_6\}$ units (i.e., d_a(O···O)) differ from that between corner-sharing $\{WO_6\}$ units (i.e., d_b(O···O)). Standard geometry optimizations logically indicate that the relative difference between d_a(O···O) and d_b(O···O) is dependent on the nature of the X centers (Figure 2). The different X centers can lead to different charge distributions within α-$[XW_9O_{33}]^{9-}$. The molecular electrostatic potentials reveal that the terminal oxo atoms in α-$[AsW_9O_{33}]^{9-}$ are the most basic, while the relative basicity lowers gradually in α-$[SbW_9O_{33}]^{9-}$ and then in α-$[BiW_9O_{33}]^{9-}$.

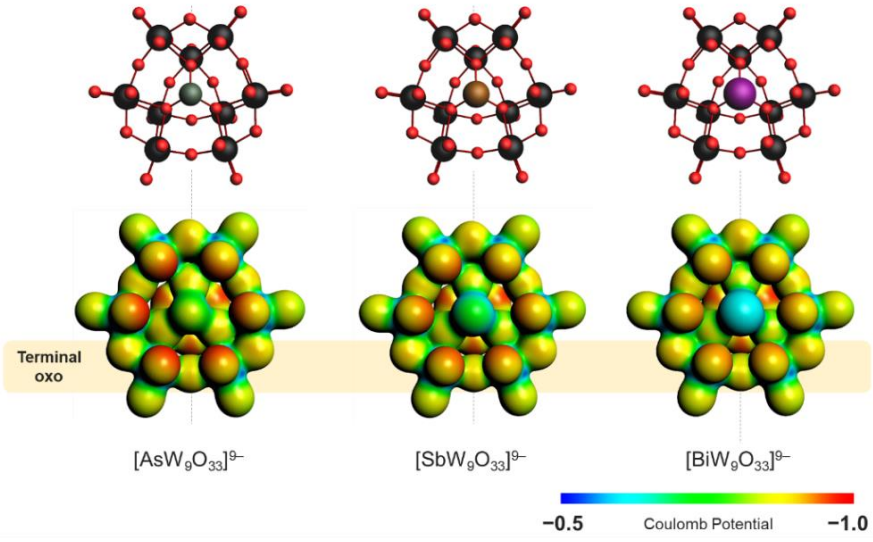

Figure 2. Ball-and-stick representation (**top**) and molecular electrostatic potential plotted over the density isosurface (**bottom**) of the three different trilacunary polyanions for qualitative comparison.

Color code: As = green, Sb = brown, Bi = violet, W = black, and O = red. The most basic sites (**bottom row**) are shown with red coloring.

Another aspect of the reactivity of α-$[XW_9O_{33}]^{9-}$ is how they connect and differ from other hetero-POTs comprised of the same building blocks. In order to discuss this aspect, we briefly focus on the chemistry of α-$[AsW_9O_{33}]^{9-}$. In aqueous media α-$[AsW_9O_{33}]^{9-}$ is relatively reactive and can bind to additional mononuclear tungstate building blocks. In the pH range between 3–4 and the presence of Na^+ cations, α-$[AsW_9O_{33}]^{9-}$ interconnects with *cis*-$[WO_2]^{2+}$ bridging units, leading to tetrameric $[Na\subseteq(WO_2)_4(\alpha\text{-}AsW_9O_{33})_4]^{27-}$ polyanions [53]. On the other hand, when the pH reaches 6 and K^+ cations are present, α-$[AsW_9O_{33}]^{9-}$ interconnects with *trans*-$[WO(H_2O)]^{4+}$ units leading to dimeric, sandwich-like $[K(H_2O)_n\{WO(H_2O)\}(\alpha\text{-}AsW_9O_{33})_2]^{13-}$ species (see Section 3) [54]. These structures show that pH and the nature of the cations have immense effect(s) upon the synthetic outcome, although, to date, their exact role in the particular self-assembly process is not clear [55].

Interaction of α-$[XW_9O_{33}]^{9-}$ with heterometals (M) can lead to a wide range of structures differing in terms of POM ligands and interconnecting heterometal centers. As the trilacunary α-$[XW_9O_{33}]^{9-}$ are polydentate ligands, their combination with high-coordinate cations (e.g., lanthanides or actinides) can result in many possible connectives and occasionally in oligomeric POM assemblies with impressive tungsten nuclearities [56]. However, for improved synthetic and structural control, trilacunary α-$[XW_9O_{33}]^{9-}$ have often been reacted with transition metal cations that have more modest coordination numbers, ultimately leading to a lower number of connecting possibilities.

If the metal cations are partially protected with non-labile ligands, they typically coordinate and saturate the lacunary site of α-$[XW_9O_{33}]^{9-}$ POM, leading to metal-functionalized Janus-like nanomolecules. However, many transition metal cations deriving from simple metal salt precursors (e.g., chlorides, nitrates, etc.) can offer up to four coordination sites in square planar orientation and thus can interconnect two α-$[XW_9O_{33}]^{9-}$ units in an archetype that, due to historical reasons, is referred to as Hervé-type POM sandwich [48]. For a more profound discussion here, we describe the Hervé-type sandwich as a linear POM assembly where a cationic $\{M_{6-x}\}$ belt (x = 0–5) is sandwiched between two α-$[XW_9O_{33}]^{9-}$ units (see Figure 3). The $\{M_{6-x}\}$ belt connects to six formerly terminal–oxo ligands deriving from both α-$[XW_9O_{33}]^{9-}$ units. The $\{M_{6-x}\}$ is thus a part of a larger cyclic $\{M_{6-x}O_{12}\}$ fragment in which when x = 0, all M-centered $\{MO_4\}$ square planes or square pyramids $\{MO_4L\}$ are in edge-sharing configuration with one another. In a scenario when the $\{M_{6-x}\}$ belt is fully saturated (i.e., x = 0), one formally distinguishes between two configurational isomers obtained because of the orientation of the $\{XO_3\}$ units. When both units $\{XO_3\}$ are oriented in an eclipsed fashion, the edge-sharing $\{WO_6\}$ octahedra from both α-$[XW_9O_{33}]^{9-}$ units are also eclipsed (i.e., *syn*). The eclipsing provides differences in interatomic $d_{(O\cdots O)}$ distances and enforces an ideal D_{3h} symmetry point group. The *syn* orientation is thus dominant among inter-POM bridging with three metal centers. However, the remaining sites in a "saturated M_6" scenario can often be occupied by metal cations with different coordination or ligand environments (e.g., alkali Na^+ and K^+).

When the two $\{XO_3\}$ units are in staggered (i.e., *anti*-) orientation, the remaining edge-sharing $\{WO_6\}$ octahedra are also staggered, and this enforces the lacunary sites to conform to a more "uniform" connectivity, which leads to an ideal $\{M_6O_{12}\}$ hexagonal belts (Figure 3). This is a profound difference and favors complete belt saturation. However, between the two very distinct sandwich archetypes $\{M_3(\alpha\text{-}XW_9O_{33})_2\}$ D_{3h} and $\{M_6(\alpha\text{-}XW_9O_{33})_2\}$ D_{3d}, there are obviously other scenarios where 2, 4, and 5 metal centers are being sandwiched between α-$[XW_9O_{33}]^{9-}$. In many of these configurations, partial occupancy or coordination changes induced by auxiliary ligands or other factors play a role that leads to different configurations, although from what we have reviewed here, the *syn* orientation is far more common than the *anti*. In most of the structures discussed, the linear alignment enforces closer proximity of the M centers, which in the case of spin-polarized centers can lead to interesting magnetic interactions and behavior.

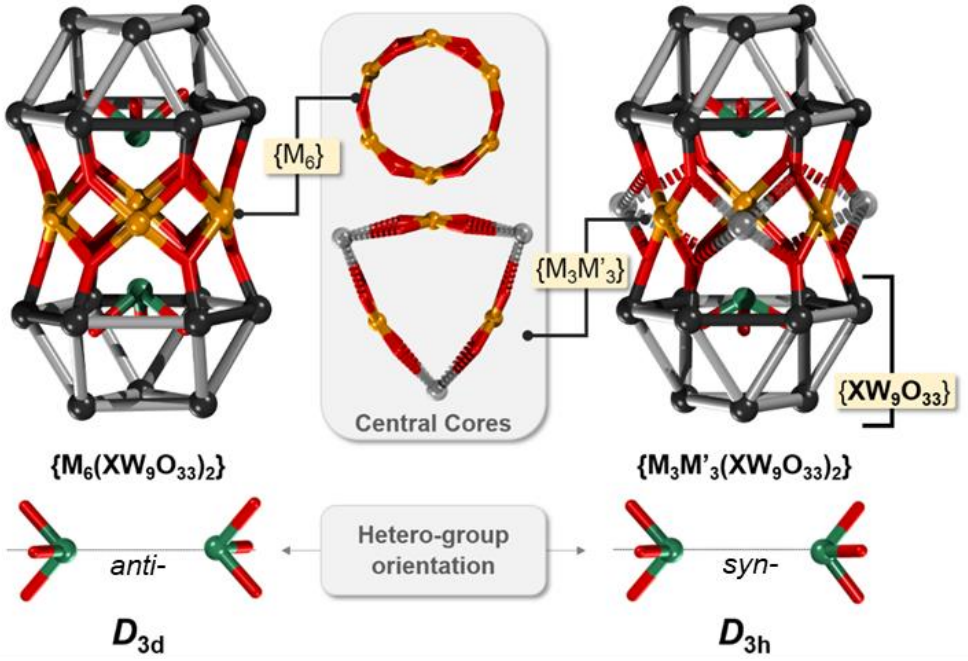

Figure 3. Ball and wireframe representation of the linear/Hervé-sandwich $\{M_6(\alpha\text{-}XW_9O_{33})_2\}$ (**left**) and $\{M_3M'_3(\alpha\text{-}XW_9O_{33})_2\}$ archetype (**right**). The sandwiched $\{M_6\}$ and $\{M_3M'_3\}$ cores are shown in between, and the orientation of the two $\{XO_3\}$ units on the bottom. In the $\{XW_9O_{33}\}$ units, all oxo ligands except those participating in the sandwiching of the central belt cores have been omitted. Color code: X = green, W = black, and O = red. For gray and black wire, coloring is used to indicate corner and edge-sharing $\{WO_6\}$ octahedra.

The last profound change in the formation of complex assemblies is the isomerization of the α-$[XW_9O_{33}]^{9-}$ to β-$[XW_9O_{33}]^{9-}$ (see Figure 1). While in the presence of transition metal cations, α-$[XW_9O_{33}]^{9-}$ condensates in linear sandwich assemblies, the condensation of β-$[XW_9O_{33}]^{9-}$ favors an offset-sandwich assembly vis-à-vis $\{M_4O_{10}(XW_9O_{33})_2\}$, commonly referred to as the Krebs-type POMs [46,57]. The offset Krebs-type POM creates a belt of four centers forming a virtual rhomboid described by two geometrically inequivalent metal centers (a-site and b-site) placed along three different interatomic distances d_1 connecting a-b centers, d_2 connecting a-a centers, and d_3 connecting b-b centers as shown in Figure 4. The two most distant corners (i.e., those connected along d_2) are typically occupied by 3d centers, while the remaining directly bridging the β-$[XW_9O_{33}]^{9-}$ can be 3d transition metal or W-based. In the Krebs-type structures, the spin-polarized centers are often distant from one another and typically exhibit very weak or no magnetic coupling interactions.

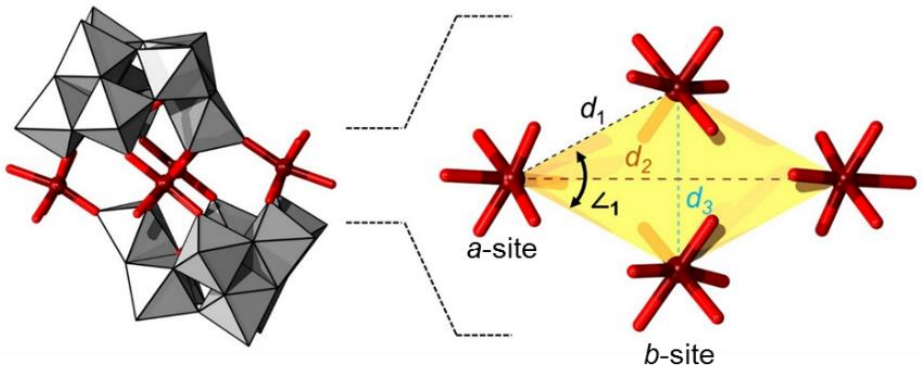

Figure 4. Offset/Krebs-type sandwich archetype $\{M_4O_{10}(\beta\text{-}XW_9O_{33})_2\}$ (**left**) and its central rhomboidal core (**right**) emphasizing the different *a*- and *b*-sites and d_1, d_2 and d_3 interatomic distances. Color code: X = green (but covered), M = brown, $\{WO_6\}$ = gray octahedra, and O = red.

3. Hervé-Type Dimers

3.1. Atypical Hervé Polyanions

In 2001, Kortz and coworkers reported the sandwich type $[\{M^{II}_2(H_2O)_2\}\{WO\}(\alpha\text{-}AsW_9O_{33})_2]^{10-}$ where M = Mn^{II}, Co^{II}, Zn^{II} (Figure 5a) [58]. In contrast to the classical Hervé-type POMs, this derived assembly incorporates only two heterometals, while a tungsten center acts as another linking group between the two α-$\{As^{III}W_9O_{39}\}$ units. Single crystal X-ray diffraction analysis revealed 79, 73, and 77% occupancy in the belt region for Mn, Co, and Zn, respectively. Elemental analysis revealed that, on average, two of the three belt positions of the dimeric polyanions are occupied by the first-row transition metal (Co, Mn, and Zn) and a tungsten atom occupies the remaining position. The M–O bond distances for the polyanions range from 1.977 to 2.343, 1.95 to 2.284, and 1.967 to 2.227 Å for Mn, Co, and Zn, respectively.

An "open-sandwich" structure has been reported by Hussain and coworkers, viz. $[\{Ni(H_2O)_4\}_2\{WO(H_2O)\}(\alpha\text{-}AsW_9O_{33})_2]^{10-}$ (Figure 5b) [59]. The latter structure is based upon the $\{(WO(H_2O))(\alpha\text{-}AsW_9O_{33})_2\}$ moiety, wherein two of the α-$\{As^{III}W_9O_{39}\}$ units are joined at one corner with an octahedrally coordinated $\{WO_5(H_2O)\}$. The polyanion consists of two nickel atoms and one sodium atom coordinated to one of the α-$\{As^{III}W_9O_{39}\}$ units. The sodium cation acts as a bridge between the two metal atoms. The other α-$\{AsW_9O_{39}\}$ unit does not bond with nickel atoms but connects to the nickel coordinated α-$\{AsW_9O_{39}\}$ Keggin unit via the $\{WO_5(H_2O)\}$ group, thus having a nominal C_{2V} symmetry. The Ni–O distances in this polyanion range from 2.03 to 2.09 Å. Magnetic studies performed upon the polyanion using a vibrating-sample magnetometer show paramagnetic behavior with the effective magnetic moment value calculated from data to be 3.23 B.M. (Bohr Magneton).

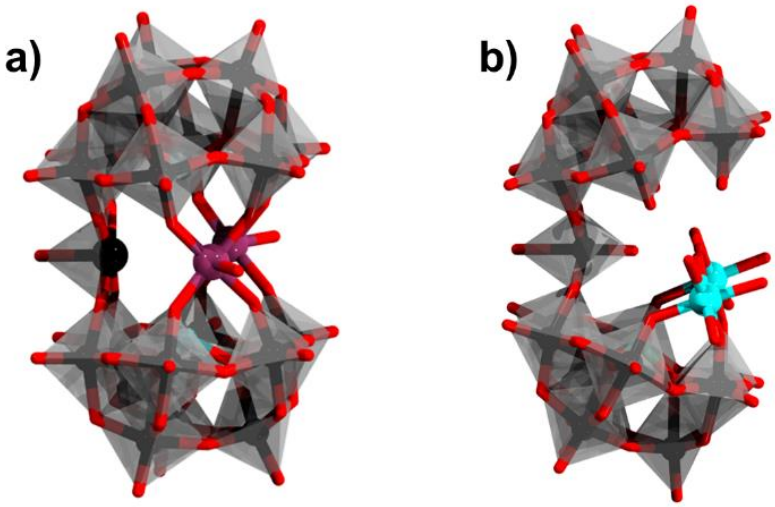

Figure 5. (**a**) $[\{Co_2(H_2O)_2\}\{WO\}(\alpha\text{-}AsW_9O_{33})_2]^{10-}$; (**b**) $[\{Ni(H_2O)_4\}_2\{WO(H_2O)\}(\alpha\text{-}AsW_9O_{33})_2]^{9-}$. Color code: As = green, Co = purple, Ni = cyan, $\{WO_6\}$ = gray octahedra, W = black, and O = red. Hydrogen atoms from aqua ligands are omitted.

3.2. Hervé Polyanions Sandwiching Three Heterometals

3.2.1. Aqua Terminating Ligands

In 1982, Hervé and coworkers reported the polyanion $[Cu_3(H_2O)_2(As^{III}W_9O_{39})_2]^{12-}$, consisting of a trimeric assembly of Cu^{II} atoms, arranged in the pattern of an isosceles triangle (Cu···Cu distances = 4.669 and 4.707 Å), sandwiched between two α-$\{AsW_9O_{39}\}$ units [48]. Interestingly, the two α-$\{As^{III}W_9O_{39}\}$ subunits are not observed to face each other exactly. The three Cu^{II} atoms are not equivalent in the polyanion, with two of the Cu^{II} ions having a square planar geometry coordinated with oxygens from the polyanion units, while one Cu^{II} ion having a square pyramidal geometry with additional oxygen at

the axial position. The Cu–O bond distances in this polyanion are in the range of 1.87–2.39 Å. The magnetic properties of this compound, reported in 1988, showed intramolecular anti-ferromagnetic coupling between the Cu atoms with $J = -7.5$ K (~ -5.2 cm^{-1}) [60].

In 2001, the latter species were revisited when a group of $[(\alpha\text{-}XW_9O_{33})_2M_3(H_2O)_3]^{12-}$, where M = Cu^{II}, Zn^{II}; X = As^{III}, Sb^{III} was reported (Figure 6a) [58]. The principal difference in the formation of $[(M(H_2O)_3)_3(\alpha\text{-}AsW_9O_{33})_2]^{12-}$ (pH range = 6.2–6.9) versus $[(M(H_2O))_2(WO(H_2O))(\alpha\text{-}AsW_9O_{33})_2]^{10-}$ (pH range = 3.9–4.8) is the pH maintained during synthesis. The Cu–O bond distances in this polyanion were also reported to be in the range of 1.87–2.39 Å. Analogous derivatives with Se^{IV} and Te^{IV} also with Cu^{II}, $[(Cu(H_2O))_3(\alpha\text{-}XW_9O_{33})_2]^{10-}$ (X = Se^{IV}, Te^{IV}) were also reported in the same article. The sandwich-type assembly in this polyanion joining the two α-$[XW_9O_{33}]^{9-}$ units are also made of three isolated Cu^{II} atoms. However, unlike the previously reported polyanions, in $[\{M(H_2O)_3\}_3(\alpha\text{-}AsW_9O_{33})_2]^{12-}$ [58], all the transition metals possess a square-pyramidal coordination geometry having four equatorial oxygens from the base polyanion units and one terminally coordinated water molecule at the axis, which now results in an idealized D_{3h} symmetry for the title polyanions. The transition metals are now observed to be bridged with each other by sodium ions in the solid-state structure. Magnetic susceptibility data indicate a single anti-ferromagnetic spin-exchange constant J for the triangular $\{Cu_3\}$ belts with $J = -1.36$ cm^{-1} for $[(Cu(H_2O))_3(\alpha\text{-}AsW_9O_{33})_2]^{12-}$ [61–63]. Representative magnetic susceptibility behavior has been shown in Figure 6b.

The antimony derivative $[(Cu(H_2O))_3(\alpha\text{-}SbW_9O_{33})_2]^{12-}$ has been synthesized by reactions of α-$[SbW_9O_{33}]^{9-}$ with $CuCl_2{\cdot}2H_2O$, or alternatively with $CuNO_3{\cdot}3H_2O$, in aqueous media under heating [64–66]. In the latter structure, the Cu^{II} centers are in square pyramidal coordination surrounded by four bridging oxo and a single terminal aqua ligand. As Cu^{II} is a d^9 complex with one unpaired electron, magnetically this sandwich POM can be considered somewhat similar to $[(V^{IV}O)_3(\alpha\text{-}SbW_9O_{33})_2]^{12-}$ derivative. The anti-ferromagnetic coupling constant $J = -1.04$cm^{-1}, while the ground state of the structure is S = 1/2. Magnetic hysteresis shows that the sandwich POM can be excited to the S = 3/2 level [61,67]. By formal exchange of Sb center with other p block elements, it has been shown that magnetization can be minorly altered [61,67]. The $[(Cu(H_2O))_3(\alpha\text{-}SbW_9O_{33})_2]^{12-}$ has also been found to act as a modular component for the formation of hybrid inorganic–organic networks materials synthesized in the presence of 4-amino-1-hydroxy-butyl-1,1-bisphosphonate ligands [68].

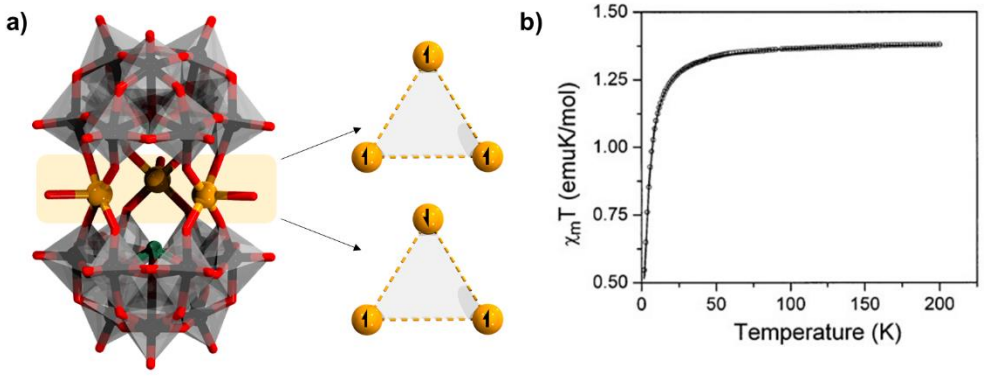

Figure 6. (**a**) Representation of $[(Cu(H_2O))_3(\alpha\text{-}SbW_9O_{33})_2]^{12-}$ and depiction of the two spins triangles as ground and excited states on the three Cu^{II} sandwiched heterometals; (**b**) representative magnetic susceptibility plot ($\chi_m T$ vs. T at H = 1000) for $\{(Cu(H_2O))_3(\alpha\text{-}XW_9O_{33})_2\}$ (X = As, Sb, Se, and Te) reproduced with permission from reference [68] published by Wiley. Color code: X = green (but covered), M = brown, $\{WO_6\}$ = gray octahedra, W = black, and O = red. Hydrogen atoms from aqua ligands are omitted.

In 2002, David and coworkers studied the bismuth derivatives and reported $[(Cu(H_2O))_3(\alpha\text{-}BiW_9O_{33})_2]^{12-}$ and $[(Mn(H_2O))_3(\alpha\text{-}BiW_9O_{33})_2]^{12-}$ derivatives [69]. Measurements of magnetochemical susceptibility of $[(Cu(H_2O))_3(\alpha\text{-}BiW_9O_{33})_2]^{12-}$ have been carried out; however reported in the literature[70] and based on limited information and reference missing, it is not clear what model was used to fit the magnetic behavior. EPR measurements of $[(Cu^{II}(H_2O))_3(\alpha\text{-}BiW_9O_{33})_2]^{12-}$ revealed the anti-ferromagnetic coupling between the Cu^{II} ions involve spin frustration, leading to a doubly degenerate S = 1/2 ground states (EPR inactive) and an S = 3/2 excited state (EPR active) [71]. In $[(Mn(H_2O))_3(\alpha\text{-}BiW_9O_{33})_2]^{12-}$, the Mn···Mn interatomic distances are in the range of 4.2–5.1 Å, which makes the dipolar interactions be smaller than the superexchange. The EPR spectra of $[(Mn(H_2O))_3(\alpha\text{-}BiW_9O_{33})_2]^{12-}$ revealed that each Mn^{II} ion is antiferromagnetically coupled through either the α-{BiW_9O_{33}} units or through space bipolar interactions. At the excited state of S = 7/2, the isotopic exchange constant, estimated in the temperature range of 5–225 K, is $J = -2.074$ cm^{-1} and the zero-field splitting parameters D = −0.381 cm^{-1}, E = 0.054 cm^{-1} [69].

3.2.2. Oxo Terminating Ligands

Similarly to $[(M(H_2O))_3(\alpha\text{-}AsW_9O_{33})_2]^{12-}$ (M = Mn^{II}, Co^{II}, Ni^{II}), Mialane and coworkers reported $[(VO)_3(\alpha\text{-}AsW_9O_{33})_2]^{11-}$, featuring three cationic {VO} moieties [65]. Titration of the polyanion with Ce^{IV} revealed that $[(VO)_3(\alpha\text{-}AsW_9O_{33})_2]^{11-}$ is a mixed-valent $\{V^{IV}_2V^{V}\}$ species. The terminal oxo atoms lead to shorter metal–oxygen bond lengths ca. 1.6 Å, in contrast to when a terminal aqua ligand is bonded (ca. 2.0 Å). The vanadium derivative, however, showed significant disorder on two of the three metals linking the {α-AsW_9O_{33}} units. For these two vanadium atoms, the V = O bonds are directed alternatively towards the inside or the outside of the sandwich interior (Figure 7). Magnetic studies on the polyanions reveal anti-ferromagnetic interactions between the metal centers with coupling constants $J = -2.9$ cm^{-1}.

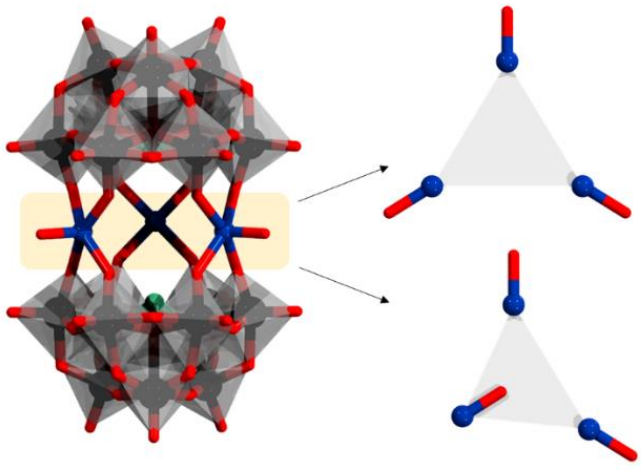

Figure 7. $[(V^{IV}O)_3(\alpha\text{-}AsW_9O_{33})_2]^{12-}$ (**left**) and the two different orientations of the cationic {VO} (**right**). Color code: X = green (but covered), V = dark blue, {WO_6} = gray octahedra, W = black, and O = red.

In 2001, Yamase reported the synthesis of the polyanion $[(V^{IV}O)_3(\alpha\text{-}SbW_9O_{33})_2]^{12-}$ [72]. This POM was obtained from the reaction of $[\alpha\text{-}SbW_9O_{33}]^{9-}$ and $VOSO_4{\cdot}5H_2O$ in aqueous sodium acetate buffer at pH 4.8. In the later structures, the vanadium centers appear as {VO_5} square pyramids, and in such form, they normally can undergo reversible redox processes between vanadium(IV) and vanadium(V). Based on circular voltammetry, it was indeed shown that $[(V^{IV}O)_3(\alpha\text{-}SbW_9O_{33})_2]^{12-}$ can undergo three one-electron oxida-

tions, that is, forming the diamagnetic $[(V^{V}O)_3(\alpha\text{-}SbW_9O_{33})_2]^{12-}$ species. The cyclic voltammogram is quasi-reversible, which suggests that the POM retains its structural integrity in the solution. In the ground state, the sandwiched core of $[(V^{IV}O)_3(\alpha\text{-}SbW_9O_{33})_2]^{12-}$ is virtually identical to that reported for the arsenic analogue (Figure 7). In the $[(V^{IV}O)_3(\alpha\text{-}SbW_9O_{33})_2]^{12-}$ sandwich structures, the interatomic $V^{IV}\cdots V^{IV}$ distances are 5.4–5.5 Å. Owing to the geometric frustration of the three centers, the particular POM shows a ground state of S = 1/2. Based on magnetic hysteresis, it has been shown that magnetization of the POM can cross from S = 1/2 level to S = 3/2. The later step is associated with a half-step magnetization, which normally is expected for an anti-ferromagnetic spin triangle [73]. The Yamase group also studied the spin frustrated $[(VO)_3(\alpha\text{-}BiW_9O_{33})_2]^{12-}$ [73,74]. The authors observed an unusual phenomenon of the magnetization of $[(VO)_3(\alpha\text{-}BiW_9O_{33})_2]^{12-}$, which jumps with distinct hysteresis for the S = 1/2 ↔ S = 3/2 levels, crossing under fast sweeping pulsed magnetic field (~10^3 T/s) at the low temperature of 0.5 K and shorter pulse field. This hysteresis is expected for an anti-ferromagnetic spin triangle with anti-symmetrical Dzyaloshinky–Moriya interactions. The level-crossing field estimated zero-field splitting energies of 5–7 K between S = 1/2 and S = 3/2 states for both polyanions for the magnetization.

3.2.3. Other Types of Terminating Ligands

When other N- or O-terminating organic ligands are present as part of the synthesis course, these ligands may coordinate with the three sandwiched heterometals. The coordinating ligand may or may not lay in the same plane as the rest of the three heterometal centers showing a form of conformational isomerism.

Termination with pyridine (pyr, C_5H_5N) has been manifested in the preparation of $[(Ni(pyr))_3(\alpha\text{-}AsW_9O_{33})_2]^{12-}$ polyanion (Figure 8a) [75]. In this polyanion, the terminal Ni−N bond distance is 2.016 Å, while the pyridine ligands lay in the same plane as the three heterometals. Magnetic susceptibility measurements have shown that the Ni^{II} cations are not fully equivalent, leading to ferromagnetic Ni···Ni exchange as depicted by J = 6.17 cm^{-1}. Similar to pyridine, functionalization with aminopyrazine (apyr) also forms products through direct coordination of nitrogen-atom with the metal, as manifested in the polyanion $[(Ni(apyr))_3(\alpha\text{-}SbW_9O_{33})_2]^{12-}$ [76]. In the latter antimonate derivative, the derived coupling constants J_1 = −0.39 cm^{-1}, J_2 = −1.07 cm^{-1} are small and negative, indicating that the Ni···Ni exchange interactions are weak anti-ferromagnetic [76].

Derivatives of 1,2,4-triazole (taz) have been reported for a number of polyanions $[(M(Htaz))_3(AsW_9O_{33})_2]^{9-}$ where M = Mn^{II}, Co^{II}, Ni^{II} (Figure 8b) [77]. The latter polyanions show weak $M^{II}\cdots M^{II}$ ferromagnetic exchange interactions with $J_{Mn\cdots Mn}$ =−0.36 cm^{-1}, $J_{Co\cdots Co}$ = 5.93 cm^{-1}, and $J_{Ni\cdots Ni}$ = 10.32 cm^{-1} [77]. Similarly, the binding of imidazole (imi) has been largely explored, leading to anti-ferromagnetic systems of $[(M(imi))_3(\alpha\text{-}SbW_9O_{33})_2]^{12-}$ where M = Mn^{II}, Ni^{II}, Co^{II}, Fe^{II}, and Cu^{II}. The Mn^{II}, Ni^{II} and Co^{II} derivatives are obtained through the interaction of $Na_2WO_4{\cdot}2H_2O$ and $SbCl_3{\cdot}6H_2O$ (or alternatively Sb_2O_3) with the transition heterometal salt in the presence of imidazole [78,79]. The latter strategy does not work for creating copper derivatives, [80] and there, the synthesis is based on the trilacunary α-$[SbW_9O_{33}]^{9-}$ [81]. The Fe^{II} derivatives are also made using α-$[SbW_9O_{33}]^{9-}$, but the iron comes as Fe^0 from iron powder in sodium acetate buffer [82]. Imidazole derivatives are also known based on the α-$[BiW_9O_{33}]^{9-}$ unit. The polyanion $[(Co(imi))_3(\alpha\text{-}BiW_9O_{33})_2]^{12-}$ has been reported to appear as a product where copper-based {Cu(imi)$_4$} is grafted on the surface of the polyanion [83]. Magnetic susceptibility studies of $[(Co(imi))_3(\alpha\text{-}BiW_9O_{33})_2]^{12-}$ shows $J_{Co\cdots Co}$ = −19.2(4) cm^{-1} assuming g = 2.005(2) and θ = −1.18(5) K, indicating anti-ferromagnetic behavior.

The use of 1-methylimidazole (mimi) has also led to the interesting derivatives, $[\{M(mimi)\}_3(\alpha\text{-}XW_9O_{33})_2]^{12-}$ where M = Co^{II}, Mn^{II} and X = Sb and Bi [84,85]. These derivatives show flexibility in the orientation of the imidazole ring in respect to the heteroatom plain (dihedral angle in the range of 13.7° to 89.7°). Magnetic susceptibility in the temperature range 2−300 K for $[(Co(mimi))_3(\alpha\text{-}BiW_9O_{33})_2]^{12-}$ showed J = −0.053 cm^{-1} and g = 2.02,

whole for $[(Mn(mimi))_3(\alpha\text{-}BiW_9O_{33})_2]^{12-}$ $J = -0.06$ cm^{-1} and g = 1.99) have shown anti-ferromagnetic interaction. Coordination of outer acetate ligands has been recorded in $[(Mn(COOH))_3(\alpha\text{-}AsW_9O_{33})_2]^{15-}$ (Figure 8c) [86]. Magnetic susceptibility studies for these polyanions showed $J = -0.07$ cm^{-1} indicating a weak anti-ferromagnetic coupling between the Mn^{II} centers [86].

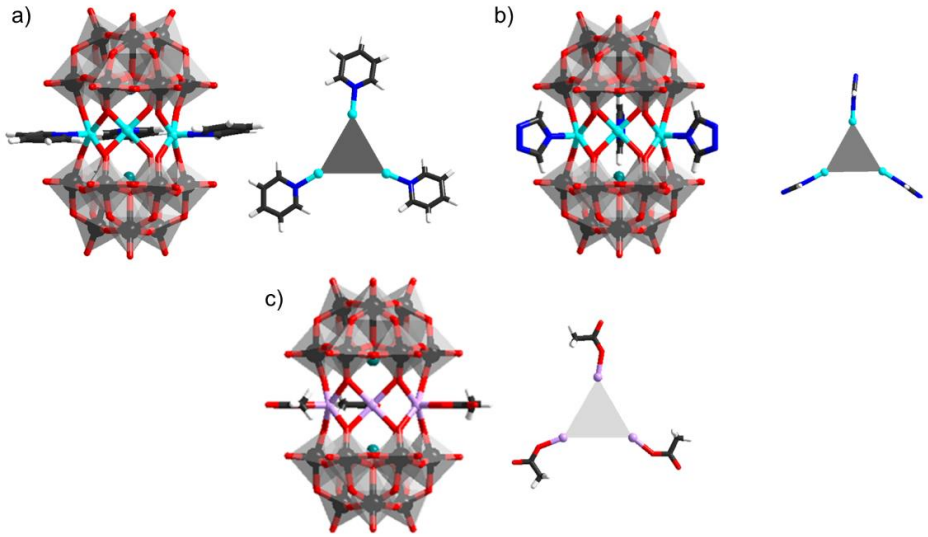

Figure 8. Polyanions and their heterometallic cores: (**a**) $[(Ni(py))_3(AsW_9O_{33})_2]^{12-}$; (**b**) $[(M(Htaz))_3(AsW_9O_{33})_2]^{9-}$; (**c**) $[(Mn(COOH))_3(AsW_9O_{33})_2]^{15-}$. Color code: As = green, Ni = cyan, Mn = light pink, H = white frame, C = dark gray frame, {WO_6} = gray octahedra, W = black, and O = red.

3.3. Hervé Polyanions Sandwiching Two and Four Heterometals

Following the discussion on the *syn*- and *anti*- scenarios discussed in Figure 3 that apply for three and six heterometal sandwiching architectures, here we discuss the sandwiching of two and four heterometals. Considering a D_{3d}-symmetrized anti scenario, populating with two centers will lead to three different configurational isomers (see Figure 9). On the other hand, using the same topology, populating with four metal centers will similarly lead to three different isomeric configurations representing reversed populations. In case anti-isomerism is switched with *syn*-orientation, then distortion between the centers may occur.

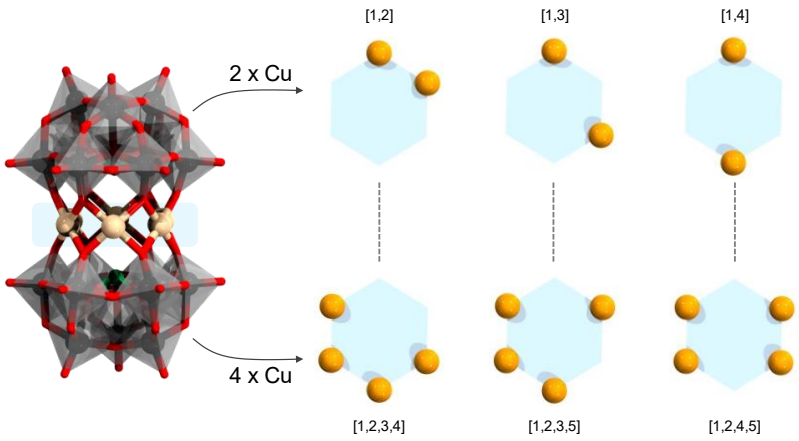

Figure 9. Generic sandwich {$Cu_n(\alpha\text{-}XW_9O_{33})_2$} (**left**); isomers when n = 2 (**top**, **right**) and n = 4 (**bottom**, **right**). Color code: X = green, partially occupied Cu = light orange, fully-occupied Cu = orange, {WO_6} = gray octahedra, W = black, and O = red.

The polyanion $[Cu_2(\alpha\text{-}SbW_9O_{33})_2]^{14-}$, obtained by the reaction of $Na_2WO_4{\cdot}2H_2O$, Sb_2O_3 and copper precursor in the presence of ethylenediamine, is an example of Hervé polyanion sandwiching two metal centers [87]. The involved ethylene diamine is not part of the Hervé motif but a chelating agent to Cu^{II} cations [87]. It is not clear to what extent ethylene diamine coordinating to free Cu^{II} affects the active concentrations leading to two heterometal sandwiches. The resolved crystal structure of $[Cu_2Na_4(\alpha\text{-}SbW_9O_{33})_2]^{10-}$ indicates that sodium and copper cations are partially distributed around the six-metal belt, implying that the three isomer configurations may be possible. On the basis of magnetic susceptibility data for $[Cu_2(\alpha\text{-}SbW_9O_{33})_2]^{14-}$ it has been concluded that there are dominant ferromagnetic coupling interactions [16].

The reversed heterometal populated sandwich $[Cu_4(\alpha\text{-}SbW_9O_{33})_2]^{10-}$ has been under hydrothermal conditions in the presence of diethylenetriamine [88]. Crystallographic study indicates that in the latter POM, the scenario where pairs of $\{Cu_2O_6\}$ units sandwiched opposite to one another is prevalent [88]. Magnetic susceptibility data of $[Cu_4(\alpha\text{-}SbW_9O_{33})_2]^{10-}$ revealed weak anti-ferromagnetic coupling [88].

Using α-$\{As^{III}W_9O_{39}\}$ and Cu^{II} ion, the polyanion $[Cu_4(H_2O)_4(\alpha\text{-}AsW_9O_{33})_2]^{10-}$ has also been reported [89]. The latter POM exhibits *syn* orientation where three copper oxo bridged cations are separated by two potassium cations from the remaining copper centers (Figure 10). Owing to the *syn* orientation, in comparison to the more idealized scenario (Figure 9), the heterometallic core of $[Cu_4(H_2O)_4(\alpha\text{-}AsW_9O_{33})_2]^{10-}$ appears slightly more distorted (Figure 10). However, the overall symmetry remains C_{2v}. The Cu–O bond lengths range from 1.91 to 2.31 Å within the $\{Cu_3O_8(H_2O)_9\}$ triad and from 1.95 to 2.55 Å within the isolated $\{CuO_4(H_2O)\}$ unit. Magnetic susceptibility data for the polyanion show the presence of both ferromagnetically and antiferromagnetically coupled Cu^{II} ions (J_1 = 2.78 ± 0.13 cm^{-1}, J_2 = −1.35 ± 0.02 cm^{-1}, and J_3 = −2.24 ± 0.06 cm^{-1}).

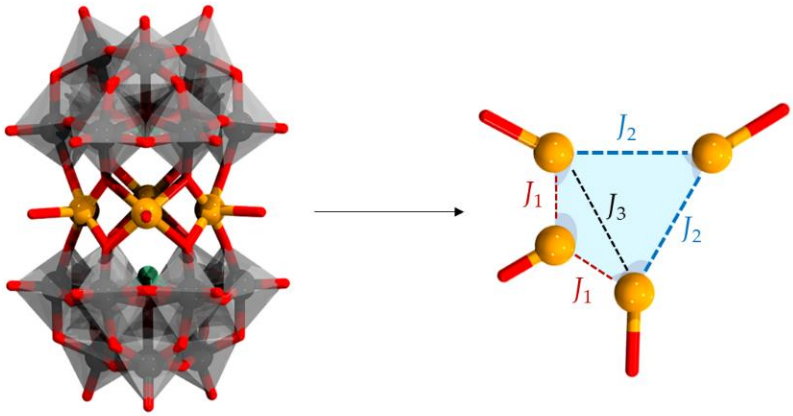

Figure 10. Polyanion $[Cu_4(H_2O)_4(\alpha\text{-}AsW_9O_{33})_2]^{10-}$ (**left**) and its $\{Cu\}_4$ core (**right**) depicting three different couplings (J_1, J_2 and J_3). Color code: As = green, Cu = orange, $\{WO_6\}$ = gray octahedra, W = black, and O = red.

3.4. Hervé Polyanions Sandwiching Five Heterometals

Furnishing the synthesis with bipyridine ligands can enforce symmetry break leading to structures with a *syn* arrangement of the α-$[SbW_9O_{33}]^{9-}$ units, which instead of three, encapsulate five metal centers. Two polyanions of the type $[\{Mn(bpy)\}_2(MnCl)_3(AsW_9O_{33})_2]^{11-}$ and $[\{Mn(bpy)\}_2(MnCl)\{Mn(OH_2)\}_2(\alpha\text{-}SbW_9O_{33})_2]^{9-}$, where X = As and Sb and bpy is bipyridine, have been reported [90]. The manganese centers are connected to bipyridine, chloride, and aqua ligand (Figure 11a). The Mn–N bond distance in the arsenic derivative is 2.25 Å, and the Mn–O bond distances are in the range of 2.08–2.24 Å. Magnetic studies on the polyanion show ferromagnetic interaction between the Mn^{II} ions. On the other hand, imidazole can also lead to an unusual binding

and formation of metal-carbon bonds between Co^{II} and Ni^{II}, leading to $\{Na_{0.7}M_{5.3}(OH_2)_2(imi)_2(Himi)(\alpha\text{-}SbW_9O_{33})_2\}$ (Figure 11b), that has partial sodium occupancy [91].

Zhao and coworkers reported in 2013 a pentameric assembly of magnetically active metals with α-$[AsW_9O_{33}]^{9-}$. The polyanion $[Na\subseteq Cu_5Cl(OH_2)_3(\alpha\text{-}AsW_9O_{33})_2]^{9-}$ has a hexagonal shaped $\{Cu_5Na\}$ assembly sandwiched between the two α-$[AsW_9O_{33}]^{9-}$ units [92]. The metal ions in this sandwich, having identical square pyramidal and square planar geometry, are categorized into four distinct groups based upon their coordination environments, viz. two identical $\{CuO_4\}$, one $\{CuO_4(H_2O)\}$, two disordered $\{Cu/NaO_4(H_2O)\}$, and one $\{CuO_4Cl\}$. The Cu–O bond lengths in this polyanion range from 1.953 to 2.007 Å, while the Cu-Cl bond has a length of 2.5368 Å. Magnetic measurements for the polyanion revealed ferromagnetic exchange interactions within the $\{Cu_5\}$ core mediated by the oxygen bridges.

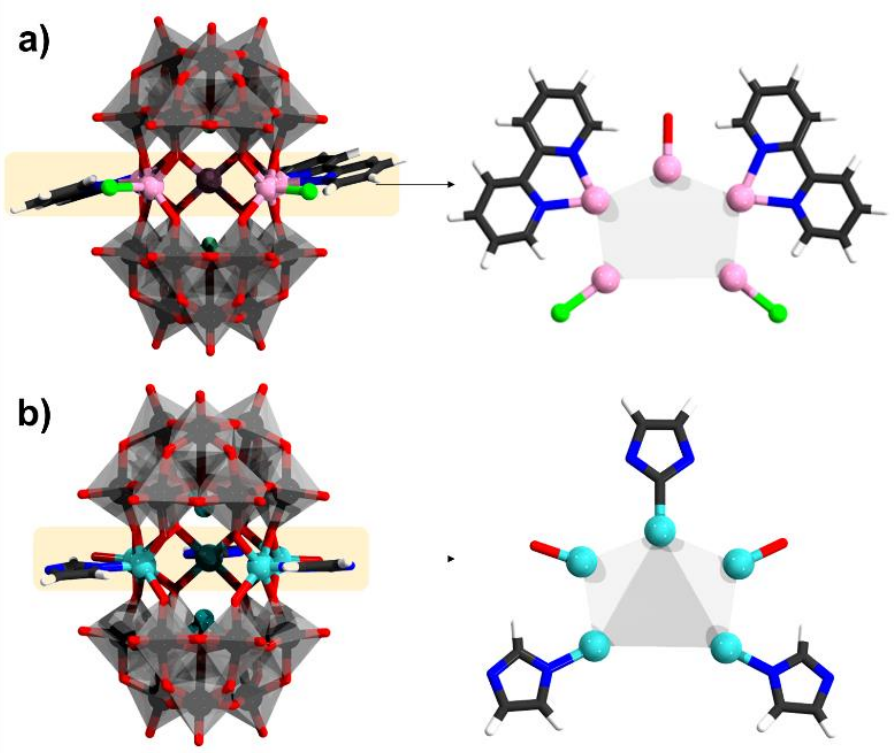

Figure 11. (**a**) $[(Mn(bpy))_2(MnCl)(Mn(OH_2))_2(\alpha\text{-}SbW_9O_{33})_2]^{8-}$; (**b**) $\{Na_{0.7}Ni_{5.3}(OH_2)_2(imi)_2(Himi)(\alpha\text{-}SbW_9O_{33})_2\}$. Color code: Sb = green (but covered), Cl = light green, Mn = pink, Ni = cyan, $\{WO_6\}$ = gray octahedra, W = black, and O = red. The partial occupancy of Na^+ has been omitted.

3.5. Hervé Polyanions Sandwiching Six Heterometals

Saturated sandwich structures with six metal centers have been reported for $[(MnCl)_6(\alpha\text{-}XW_9O_{33})_2]^{12-}$ (Figure 12a), [93] and $[(CuCl)_6(\alpha\text{-}XW_9O_{33})_2]^{12-}$ [94]. These forms of sandwich structures are prepared using similar conditions as the trimetalate Hervé-type sandwiches; however, the synthesis is typically carried out at ambient conditions, which may enhance slower sandwich closing giving time coordination between heterometals to occur. Both sandwich structures exhibit ferromagnetic coupling where for the ground state and the coupling constant values for $[(CuCl)_6(\alpha\text{-}SbW_9O_{33})_2]^{12-}$ is S = 3 and J = +29.5 cm^{-1}, and for $[(MnCl)_6(\alpha\text{-}SbW_9O_{33})_2]^{12-}$ is S = 15 and J = +0.14 cm^{-1} [94,95]. Further studies of the magnetic interactions for the polyanions $[(CuCl)_6(\alpha\text{-}AsW_9O_{33})_2]^{12-}$ and $[(MnCl)_6(\alpha\text{-}SbW_9O_{33})_2]^{12-}$ by Tsukerblat and coworkers gave coupling constants of J = 35 and 0.55 cm^{-1}, respectively, and have also emphasized the importance of axial anisotropy towards explaining the magnetic properties of such arrangements [96].

Linking of imidazole ligands produces $[M_6(imi)_6(\alpha\text{-}AsW_9O_{33}H_3)_2]$ where M = Mn^{II}, Ni^{II}, Zn^{II} (Figure 12b) [97]. Magnetic susceptibility data for the nickel gave J = +1.96 cm^{-1}, showing $Ni^{II}\cdots Ni^{II}$ ferromagnetic coupling. When instead of chloride ligands, oxalate ligands are involved, there is a possibility for the POM to grow further in the same plane with the hexametalate transition metal core. Using the oxalate addition, the ferromagnetic $[(Mn(ox))_3(Mn(H_2O)_3)_3(Mn(H_2O)_2)_2(Mn(H_2O))(\alpha\text{-}SbW_9O_{33})_2]^{6-}$ species has been isolated (Figure 12c) [98].

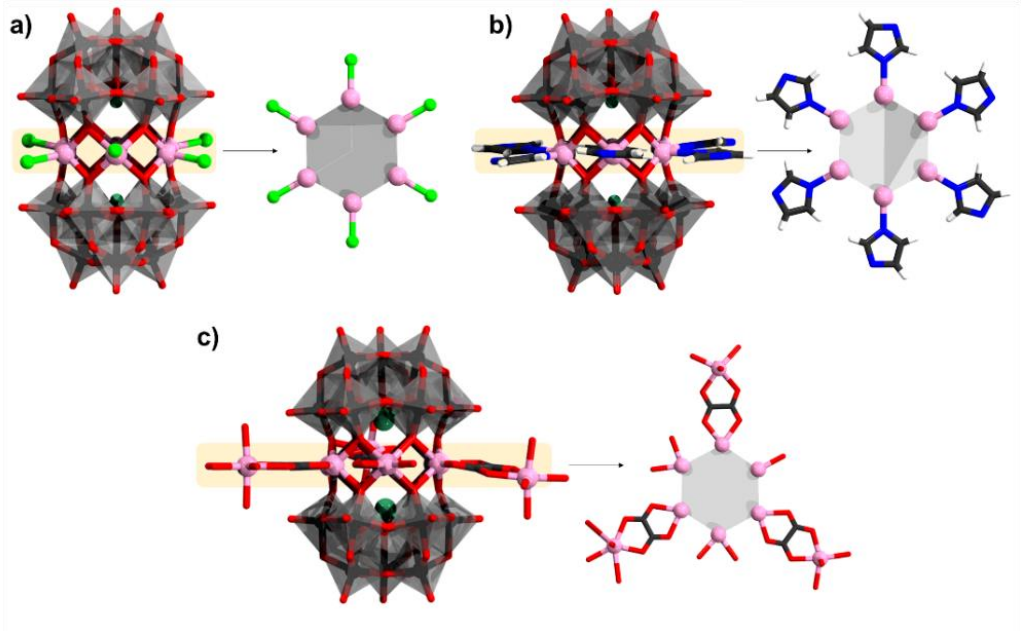

Figure 12. Polyanions and their heterometallic cores: (**a**) $[(MnCl)_6(\alpha\text{-}SbW_9O_{33})_2]^{12-}$; (**b**) $[Mn_6(imi)_6(\alpha\text{-}H_3AsW_9O_{33})_2]$; (**c**) $[(Mn(ox))_3(Mn(H_2O)_3)_3(Mn(H_2O)_2)_2(Mn(H_2O))(\alpha\text{-}SbW_9O_{33})_2]^{6-}$. Color code: As/Sb = green, Cl = light green, Mn = pink, N = blue, H = white, C = dark gray, {WO_6} = gray octahedra, W = black, and O = red. H atoms on aqua ligands are omitted.

3.6. Hervé Polyanions Sandwiching Mixed-Metallic Cores

In addition to the homometallic trimeric assemblies interspersed by alkali metal cations, several heterometallic assemblies with only transition metals and mixed transition metal-lanthanides have also been reported. One example is $[((V^{IV}O)_2Ln(H_2O)_4)(\alpha\text{-}AsW_9O_{33})_2]^{11-}$, where Ln = Dy and Gd (Figure 13a) [99,100]. The polyanion shows an idealized C_{2v} symmetry. V−O bond lengths range from ~1.6 to 1.99 Å, and the Ln–O (Ln = Dy, Gd) bond lengths range from ~2.3 to 2.8 Å. The two V^{IV} atoms in both the polyanions possess square pyramidal geometry with a short apical V = O bond of distance ~1.6 Å and are via sodium counter cations. Ln centers in square antiprism coordination. Magnetic data for the polyanions showed weak anti-ferromagnetic interactions between the vanadium (J_{VV} = −2.55 cm^{-1}) atoms and weak ferromagnetic interactions between vanadium and the lanthanide (J_{GdV} = 0.6 cm^{-1}).

Another structure is $[M(H_2O)(Ti^{IV}O)_2(\alpha\text{-}As^{III}W_9O_{33})_2]^{12-}$ where M = Co^{II}, Ni^{II}, Cu^{II}, and Zn^{II} (Figure 13b) [101]. The polyanion was synthesized by the reaction of the monovacant $[(Ti^{IV}O)_2(\alpha\text{-}As^{III}W_9O_{33})_2]^{14-}$, [102] with the respective metal. Magnetic studies on these polyanions indicate anti-ferromagnetic interactions with the nearest neighbors for these compounds, with effective magnetic moments calculated to be 5.45, 3.11, and 2.12 Bohr magnetons (B.M.) per molecule for M = Co^{II}, Ni^{II}, and Cu^{II} respectively.

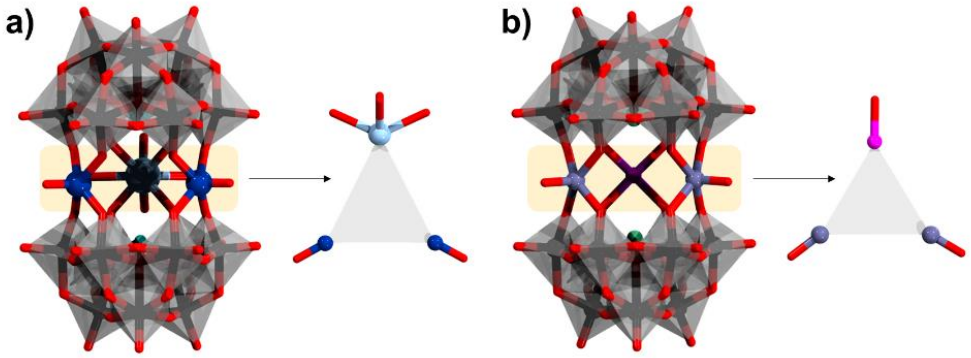

Figure 13. (**a**) $[((V^{IV}O)_2Ln(H_2O)_4)(\alpha\text{-}AsW_9O_{33})_2]^{11-}$; (**b**) $[Co(H_2O)(Ti^{IV}O)_2(\alpha\text{-}As^{III}W_9O_{33})_2]^{12-}$. Color code: As = green, Ti = dark pink, Co = violet, V = dark blue, Gd = light blue, {WO_6} = gray octahedra, W = black, and O = red. H atoms on aqua ligands are omitted.

Another is the polyanion $[Cu(H_2btp)Ln_{0.5}Na_{1.5}Cu_3(H_2O)_5(\alpha\text{-}AsW_9O_{33})_2]^{7-}$ where Ln = Ho, Yb, and btp is 1,3−bis[tris(hydroxymethyl)methylamino]propane (Figure 14) [103]. The copper-organic group is in distorted octahedral geometry binding to two O and two N units. The moiety connects to the middle pentagonal metallocycle $\{Ln_{0.5}Na_{1.5}Cu_3(H_2O)_5\}$ cluster where one position is a shared $[Ln_{0.5}/Na_{0.5}]^{2+}$ cation. The $[Ln_{0.5}/Na_{0.5}]^{2+}$ cation binds to eight oxygen atoms from the {α-AsW_9O_{33}} unit as well as two water ligands, achieving a square antiprism. The Ho/Na−O bond lengths range from 2.290 to 2.781 Å. Magnetic susceptibility data for the Ho derivative between 2 and 300 K were fitted according to the Curie–Weiss law, resulting in C = 11.21 emu K mol^{-1} and θ = 2.89 K. The small positive θ value confirms the presence of the weak $Cu^{II}\cdots Ho^{III}$ ferromagnetic interactions.

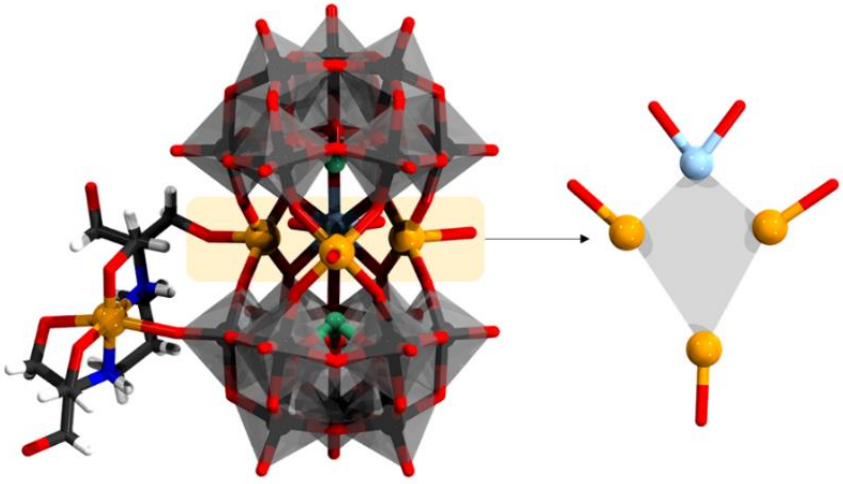

Figure 14. $[Cu(H_2btp)Ho_{0.5}Na_{1.5}Cu_3(H_2O)_5(\alpha\text{-}AsW_9O_{33})_2]^{11-}$ and its heterometallic core. Color code: As = green, Cu = orange, N = blue, H = white, C = dark gray, Ho/Na = light blue, {WO_6} = gray octahedra, W = black, and O = red. H atoms on aqua ligands are omitted.

4. Krebs-Type Dimers

4.1. Differentiation between Classical Krebs Dimers

Referring to Figure 4, we generally distinguish between *a*- and *b*- site octahedra in the Krebs structure. As noted, the interatomic distance between two a-sites (i.e., d_2) is ca. 10.0 Å, between two b-sites (i.e., d_3) it is ca. 5.6 Å, and between an a and b site (i.e., d_1) it is ca. 5.4 Å. Overall, d_1, d_2, and d_3 are relatively large interatomic distances, and thus none or only very weak magnetic exchange interactions occur in this POM archetype [104,105].

The diamagnetic Krebs structure $[(WO_2OH)_2(WO_2)_2(\beta\text{-}SbW_9O_{33})]^{12-}$ is synthesized by reacting α-$[SbW_9O_{33}]^{9-}$ with sodium tungstate in aqueous media. Early studies have

shown that the structure can be post-functionalized with 3d metal cations (e.g., Fe^{III}, Co^{II}, Mn^{II}, Ni^{II}, and Cu^{II}) [44,105]. The latter reactions lead to the formal substitution of the peripheral {WO_2OH} units with {$M(H_2O)_3)_2$} units, yielding {$(M(H_2O)_3)_2(WO_2)_2(\beta$-$SbW_9O_{33})$} derivative species which can be doubly protonated [44,105].

In addition to the typical synthetic pathways, mixtures of iron powder, imidazole, and pre-synthesized Krebs precursor $[(WO_2OH)_2(WO_2)_2(\beta$-$SbW_9O_{33})]^{12-}$ in acetic buffer solution under heating leads to the formation of the Fe^{II} derivative $[Fe^{II}_2(H_2O)_6(WO_2)_2(\beta$-$SbW_9O_{33})_2]^{10-}$ [106]. The latter structure is shown to be potential as catalyst for Fenton reaction and electrochemical sensing of ascorbic acid [106].

The Krebs-like tetrametallic archetype $[M_4(H_2O)_{10}(\beta$-$SbW_9O_{33})_2]^{n-}$ has been reported for trivalent cations such as Fe^{III}, Cr^{III}, and Al^{III} (Figure 15) [107,108]. The Fe^{III} and Cr^{III} derivative has been obtained through a reaction of respective chloride salts with trilacunary precursors α-$[XW_9O_{33}]^{9-}$ (X = As, Sb) in water at *pH* 3.0 under heating [107]. Owing to the Fe^{III} oxidation state, the polyanion $[Fe^{III}_4(H_2O)_{10}(\beta$-$SbW_9O_{33})_2]^{6-}$ is a subject to four electron reductions, which can lead to $[Fe^{II}_4(H_2O)_{10}(\beta$-$SbW_9O_{33})_2]^{10-}$ species. The latter interconversion is of relevance for catalytic oxygenation of catechol [109]. However, at the same time, it may be causing uncertainty in the accurate determination of the magnetic ground state of $[Fe^{III}_4(H_2O)_{10}(\beta$-$SbW_9O_{33})_2]^{6-}$. Based on the isotropic Heisenberg Hamiltonian model, it was proposed that the ground state of the POM salt supposedly containing $[Fe^{III}_4(H_2O)_{10}(\beta$-$SbW_9O_{33})_2]^{6-}$ has a total spin of $S = 2$ [110]; however, X-ray photoelectron Fe 2p spectra have revealed that the iron centers have Fe^{II} formal valence state [110]. This deviation from the contained Fe^{III} has been explained based on charge-transfer effects. [110]

Isolation of {Mn_4}-Krebs derivative has been achieved with the help of manganese carbonyl cations {$Mn(CO)_3$}, leading to the polyanions $[\{Mn_4(H_2O)_{10}\}\{Mn(CO)_3\}_2(\beta$-$XW_9O_{33})_2]^{8-}$ (X = Sb and Bi) [111]. Magnetic measurements of the latter compound at 1.8–300 K under a 2k Oe applied field suggest that the Mn^{II} ions are strongly antiferromagnetically coupled.

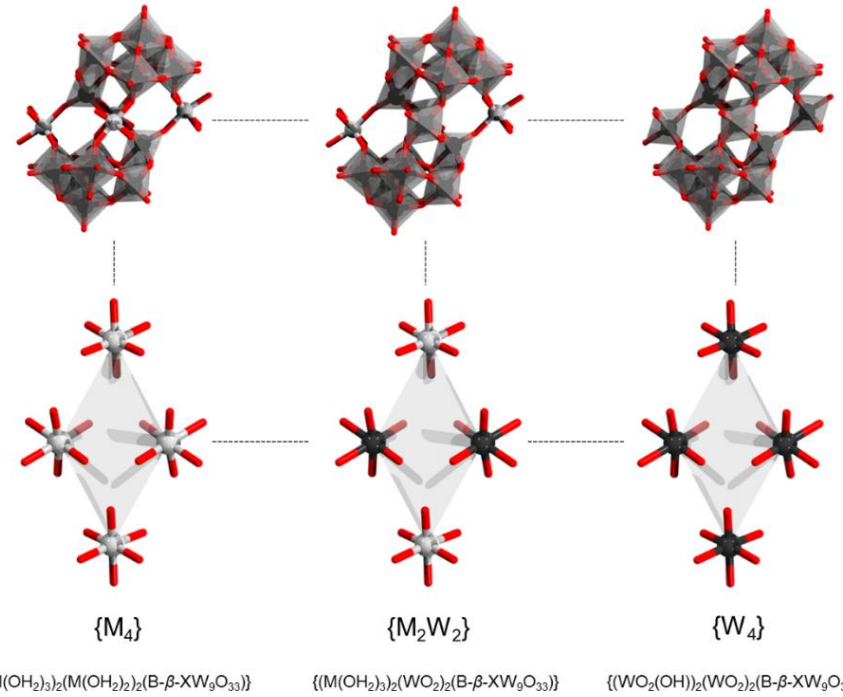

Figure 15. Offset/Krebs-type sandwich archetype (**top row**) and its sandwiched core (**bottom**) depicting full substitution with heterometals (**left**), partial substitution {M_2W_2} (**center**) and fully substitution with tungstate addenda {W_4} units (**right**). Color code: Sb = brown (but covered), M = gray, {MO_6}/{WO_6} = gray octahedra, W = black, and O = red. H atoms on aqua ligands are omitted.

4.2. Partial Substitutions in Krebs Dimers

In the solid state, some Krebs-type polyanions may reflect compositions that deviate from the scenarios $\{(M(H_2O)_3)_2(WO_2)_2(\beta\text{-}SbW_9O_{33})\}$ and $\{M_4(H_2O)_{10}(\beta\text{-}XW_9O_{33})_2\}$ shown in Figure 15. However, currently, it is not clear if these partially substituted compositions reflect averages of $\{(M(H_2O)_3)_2(WO_2)_2(\beta\text{-}SbW_9O_{33})\}$ and $\{M_4(H_2O)_{10}(\beta\text{-}XW_9O_{33})_2\}$ in the crystallographic lattice, or individual POM entities with partial substitutions indeed being formed. Examples of such polyanionic motifs in the solid state are: the discrete $[\{Mn_{3.5}W_{0.5}(H_2O)_{10}\}\{Mn(CO)_3\}_2(\beta\text{-}SbW_9O_{33})_2]^{4-}$ [111], $[Mn_{2.5}W_{1.5}(H_2O)_8(\beta\text{-}SbW_9O_{33})_2]^{4-}$ [112], and the chain-type $\{(Co(H_2O)_2)_3W(H_2O)_2(\beta\text{-}SbW_9O_{33})_2\}^{6-}$ [112]. The latter two Mn-functionalized Krebs structures exhibit weak anti-ferromagnetic coupling (θ_c = −0.056 K in the range 50–300K) [112]. A number of related species to $[(M(H_2O)_3)_2(M_{0.5}W_{0.5}O)_2(\beta\text{-}BiW_9O_{33})_2)]^{10-}$ where M = Mn^{II}, Co^{II}, Ni^{II} have been produced in the presence of triethanolamine cations [113].

4.3. Ligand Substitution in Krebs Dimers

Decorated Krebs structures can be prepared when the aqua ligands are linked to the heterometal M in $\{(M(H_2O)_3)_2(WO_2)_2(\beta\text{-}XW_9O_{33})\}$ and $\{M_4(H_2O)_{10}(\beta\text{-}XW_9O_{33})_2\}$ are exchanged. An example of such exchange is illustrated by $[Fe_2(DMSO)_8(WO)_2(\beta\text{-}XW_9O_{33})_2]^{4-}$ which has been obtained by dissolving $[(Fe(H_2O)_3)_2(WO_2)_2(\beta\text{-}SbW_9O_{33})]^{8-}$ in DMSO, and recrystallizing it in the presence of ruthenium bipyridine cations [114]. Another strategy to exchange the aqua ligands may be by introducing suitable binding ligands in the synthesis process. For instance, by introducing pyridine-3,4−dicarboxylate (pdc), the polyanion $[Fe_4(H_2O)_8(pdc)_2(\beta\text{-}SbW_9O_{33})_2]^{6-}$ (Figure 16a) has been prepared instead of $[Fe^{III}_4(H_2O)_{10}(\beta\text{-}SbW_9O_{33})_2]^{6-}$ [115]. Field-dependent magnetization measurement for $[Fe_4(H_2O)_8(pdc)_2(\beta\text{-}SbW_9O_{33})_2]^{6-}$ at 2 K indicated S = 7 ground state [115]. The addition of oxalate (ox) can similarly lead to the formation of different products depending on the reaction pH. At pH = 3.0 discrete $[Fe^{II}_4(ox)_4(H_2O)_2(\beta\text{-}SbW_9O_{33})_2]^{14-}$ (Figure 16b) polyanions are isolated, [104] while at pH = 6.0 chains of $\{Fe^{II}_4(ox)_4(\beta\text{-}SbW_9O_{33})_2\}_n$ are formed [104]. The presence of ethylenediamine during the formation process also leads of chain-like structures made of $\{Fe^{III}_4(H_2O)_8(\beta\text{-}SbW_9O_{33})_2\}$ components [104].

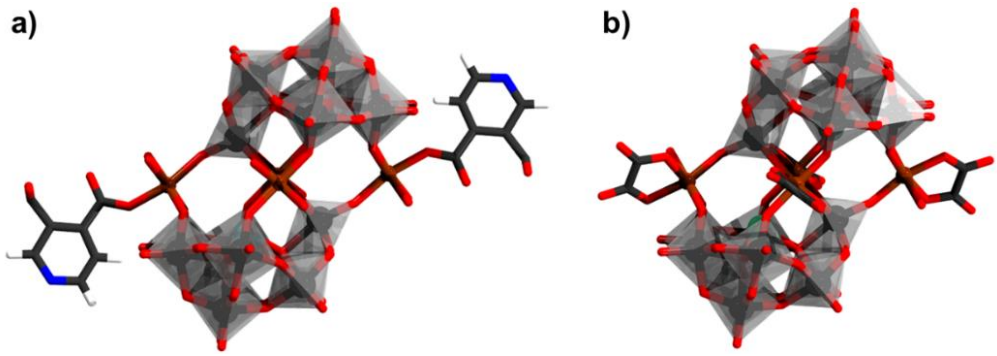

Figure 16. (**a**) $[Fe_4(H_2O)_8(pdc)_2(\beta\text{-}SbW_9O_{33})_2]^{6-}$; (**b**) $[Fe^{II}_4(ox)_4(H_2O)_2(\beta\text{-}SbW_9O_{33})_2]^{14-}$ Color code: X = green (but covered), Fe = brown, $\{WO_6\}$ = gray octahedra, W = black, and O = red. H atoms on aqua ligands are omitted.

If the added ligands are larger and have more than one binding site, then dimerization may be possible. By introducing N, O-chelating ligands such as pyrazine-2,3-dicarboxylate (pyzdc), [116] dimeric product $[(pyzdc)_2\{NaNi_2(H_2O)_4(WO_2)_2(\beta\text{-}SbW_9O_{33})_2\}_2]^{22-}$ containing two components of $[\{Ni(H_2O)_3\}_2(WO_2)_2(\beta\text{-}SbW_9O_{33})_2]^{10-}$ is obtained [117]. The dimerization is also prevalent among Krebs-type polyanions with central belt involving heterometallic centers such as Ni^{II}, Co^{II}, or Mn^{II}), [118] as or Krebs-type structures where the two tungstate metals at the a-sites are exchanged with tin heterogroups [119].

4.4. Grafting Metal Cations and Interconnecting Krebs Dimers

The incorporation of transition metals and lanthanides within a single POM stabilized structure has been seen as a viable method for designing 3d-4f complexes [120]. However, using the [α-SbW_9O_{33}]$^{9-}$ polyanion incorporating both metal centers has been challenging. One reason is that the lanthanides have larger coordination spheres and often may lack directionality. In this regard, a number of structures containing Krebs-type complexes [$Fe^{II}_4(H_2O)_{10}(\beta$-$SbW_9O_{33})_2]^{10-}$ and lanthanide cations have been reported [121]. Such compounds have been obtained through the use of 2−picolinic acid (pic), leading to [$Fe^{II}_4(H_2O)_2(pic)_4(\beta$-$SbW_9O_{33})_2]^{10-}$ species and [$Ln(H_2O)_5]^{3+}$ cations where Ln^{III} = La^{III}, Pr^{III}, Nd^{III}, Sm^{III}, Eu^{III} (Figure 17a) [121]. Using a similar strategy and threonine (thr) ligands, another series of [$Fe^{III}_4(H_2O)_8(thr)_2(\beta$-$SbW_9O_{33})_2]^{6-}$ species interconnected with [$Ln(H_2O)_8]^{3+}$ cations where Ln = Pr^{III}, Nd^{III}, Sm^{III}, Eu^{III}, Gd^{III}, Dy^{III}, Lu^{III} have been prepared [122]. Among the latter series, the Eu^{III} derivatives have shown expected fluorescent emission.

Patzke and coworkers reported a series of 0-, 1-, 2-, and 3-dimensional copper-containing tungstobismuthate polyanions [70]. The reported complexes include the discrete [$Cu_2(H_2O)_4Cl_2(\beta$-$BiW_{10}O_{35})_2]^{12-}$ and [$Cu_2(H_2O)_6(\beta$-$BiW_{10}O_{35})_2]^{10-}$ polyanions. Two-dimensional networks of {$Cu_{0.5}Cl[Cu_2(H_2O)_4(\beta$-$BiW_{10}O_{35})_2]\}^{10-}$ (Figure 17b), {$Cu[Cu_2(H_2O)_4(\beta$-$BiW_{10}O_{35})_2]\}^{8-}$, [$Cu_3(H_2O)_3(\alpha$-$BiW_9O_{33})_2]^{12-}$ and three-dimensional [$(Cu_3Cl)(K_{2.62}Cu_{0.38}(H_2O)_3(\alpha$-$BiW_9O_{33})_2]^{9-}$ have also been reported. The copper centers in these series are relatively away from one another in the range of 8 to 11 Å.

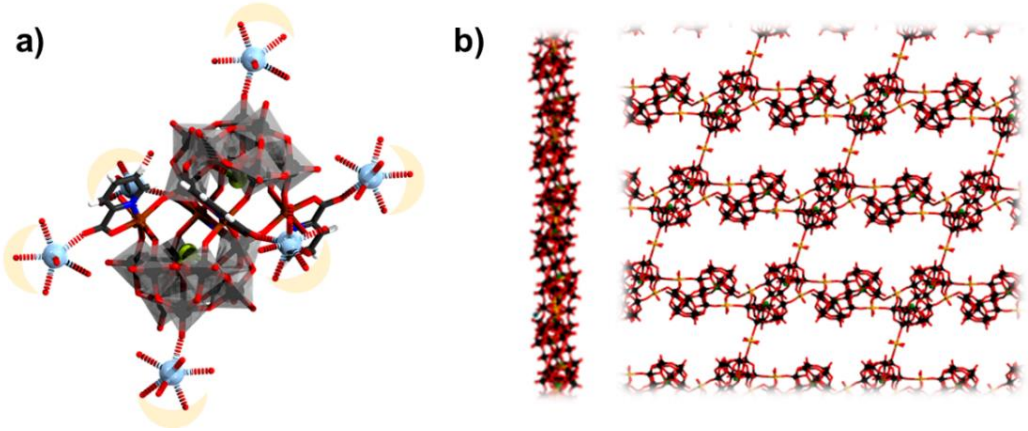

Figure 17. (**a**) La^{III} cations grafted on [$Fe^{II}_4(H_2O)_2(pic)_4(\beta$-$SbW_9O_{33})_2]^{10-}$; (**b**) side and top view on two dimensional {$Cu_{0.5}Cl[Cu_2(H_2O)_4(\beta$-$BiW_{10}O_{35})_2]\}^{10-}$. Color code: X = green (but covered), La = light blue, Fe = brown, {WO_6} = gray octahedra, W = black, and O = red. H atoms on aqua ligands are omitted.

5. Vision on POMtronics

POMtronics is a term coined in 2020 [41] that broadly refers to advanced applications of POMs deriving from their magnetic, electronic, and optical properties [123]. In a more narrow sense, POMtronics refers to POM-based nanoelectronics and spintronic devices [124]. A typical example may be a symmetrical and spherical POM sandwiched between two gold electrodes functioning as a current switch (Figure 18) [124]. Spin-polarized POMs are of special interest for molecular junction as their current transport can be influenced without the need to employ an external magnetic field [125].

Sandwich-type POMs exhibit an ellipsoidal shape, meaning that upon binding to electrodes, two or more distinguishable orientations can be adopted. A similar scenario appears for the ellipsoidal {$(SO_3)_2W_{18}O_{54}$}) POMs which have been used in POMtronics applications [126]. However, in contrast to the previous example, many Hervé dimers, as showcased in this work, have an enormous potential for broad rational derivatization and formation of magnetic POMs in their ground state. Unfortunately, to date, Hervé has rarely been used for functionalization of electronic nanosystems. In 2008, Charron et al.

reported a successful deposition of $\{Co(H_2O)(WO)_2(AsW_9O_{33})_2\}$ on a single walled nanotube [127]. More recently, the group of Kögerler demonstrated that trimeric cobalt functionalized POTs be effectively deposited through simple incubation on freshly prepared gold substrates [125].

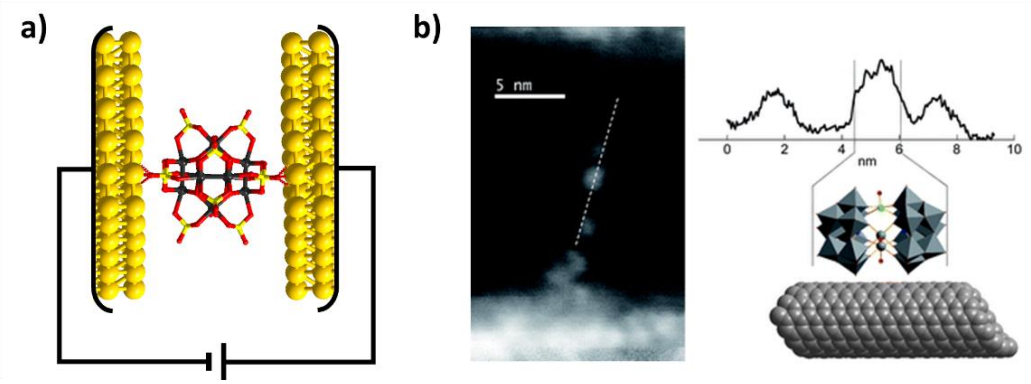

Figure 18. (**a**) Current-switching POMtronics based on $\{Pt_{12}O_8(SO_4)_{12}\}$ polyanions sandwiched between two gold electrodes as reported in refence [126]. (**b**) High-angular annular dark-field scanning transmission electron microscopy image of $\{Co(H_2O)(WO)_2(AsW_9O_{33})_2\}$ deposited over carbon nanotubes. Reproduced with permission from reference [127] published by The Royal Society of Chemistry.

6. Conclusions

The objective of this article has been to provide a comprehensive overview of the two most common sandwich-type archetypes in POM chemistry—Hervé-type and Krebs-type. The Hervé-type POMs generally adopt two main arrangements of the lacunary units and are capable to incorporate between two and six magnetic heterometals. The close arrangement of the metal centers typically causes spin interactions leading to ferromagnetic and antiferromagnetic scenarios. The relative arrangement of the lacunary units also plays role in the number of incorporated centers. Considering the synthetic conditions, these types of POM dimers can be further functionalized with a variety of binding ligand and grafting cations. The Krebs-type polyanions appear to be more common for Sb- and Bi-based lacunary heteroPOMs. In the latter polyanion, the metal centers lay further apart from one another, and thus most of the interactions between magnetic heterocenters remain weakly antiferromagnetic. Both sorts of polyanions show stability to multielectron reductions, which is not only interesting in magnetism but in catalysis as well.

With the present review we thus aimed to provide a comprehensive structuring of magnetic POM sandwich dimers, which will be extended to other POM systems in future. Although currently it may be challenging to derive rules in which one can rationally design new sandwich POMs with desired magnetic properties, current applications of knowledge engineering in chemistry [128] show promise that such endeavor to be achieved in near future. In this regard, we also envision that magnetic POM dimers would be of high interest in the development of future POM-based nanoelectronics (i.e., POMtronics) [124,129].

Author Contributions: Conceptualization, writing, review, and editing, A.K., A.B., and S.S.M. All authors have read and agreed to the published version of the manuscript.

Funding: A.K. thanks the Alexander von Humboldt Foundation and the Isaac Newton Trust for Feodor Lynen research fellowship.

Conflicts of Interest: The authors declare no conflict of interest.

Abbreviations

apyr	aminopyrazine
bpy	bipyridine
btp	1,3−bis[tris(hydroxymethyl)methylamino]propane
DMSO	dimethyl sulfoxide
imi	imidazole
mimi	1-methylimidazole
ox	oxalate
POM	polyoxometalate
POT	polyoxotungstate
pdc	pyridine-3,4−dicarboxylate
pyzdc	pyrazine-2,3-dicarboxylate
pic	2−picolinic acid
pyr	pyridine
taz	1,2,4−1H-triazole
thr	threonine

References

1. Gaita-Arino, A.; Prima-Garcia, H.; Cardona-Serra, S.; Escalera-Moreno, L.; Rosaleny, L.E.; Baldovi, J.J. Coherence and organization in lanthanoid complexes: From single ion magnets to spin qubits. *Inorg. Chem. Front* **2016**, *3*, 568–577. https://doi.org/10.1039/C5QI00296F.
2. Bertaina, S.; Gambarelli, S.; Mitra, T.; Tsukerblat, B.; Muller, A.; Barbara, B. Quantum oscillations in a molecular magnet. *Nature* **2008**, *453*, 203–206. https://doi.org/10.1038/nature06962.
3. Hill, S.; Edwards, R.S.; Aliaga-Alcalde, N.; Christou, G. Quantum coherence in an exchange-coupled dimer of single-molecule magnets. *Science* **2003**, *302*, 1015–1018. https://doi.org/10.1126/science.10900.
4. Cerletti, V.; Coish, W.A.; Gywat, O.; Loss, D. Recipes for spin-based quantum computing. *Nanotechnology* **2005**, *16*, R27–R49. https://doi.org/10.1088/0957-4484/16/4/r01.
5. Atzori, M.; Morra, E.; Tesi, L.; Albino, A.; Chiesa, M.; Sorace, L.; Sessoli, R. Quantum Coherence Times Enhancement in Vanadium(IV)-based Potential Molecular Qubits: The Key Role of the Vanadyl Moiety. *J. Am. Chem Soc.* **2016**, *138*, 11234–11244. https://doi.org/10.1021/jacs.6b05574.
6. Baldovi, J.J.; Cardona-Serra, S.; Clemente-Juan, J.M.; Coronado, E.; Gaita-Arino, A.; Palii, A. Rational design of single-ion magnets and spin qubits based on mononuclear lanthanoid complexes. *Inorg. Chem.* **2012**, *51*, 12565–12574. https://doi.org/10.1021/ic302068c.
7. Stamp, P.C.E.; Gaita-Ariño, A. Spin-based quantum computers made by chemistry: Hows and whys. *J. Mater. Chem.* **2009**, *19*, 1718–1730. https://doi.org/10.1039/b811778k.
8. Schleich, W.P. Engineering decoherence. *Nature* **2000**, *403*, 256–257. https://doi.org/10.1038/35002223.
9. Escalera-Moreno, L.; Baldovi, J.J.; Gaita-Arino, A.; Coronado, E. Spin states, vibrations and spin relaxation in molecular nanomagnets and spin qubits: A critical perspective. *Chem. Sci.* **2018**, *9*, 3265–3275. https://doi.org/10.1039/c7sc05464e.
10. Donati, F.; Rusponi, S.; Stepanow, S.; Wäckerlin, C.; Singha, A.; Persichetti, L.; Baltic, R.; Diller, K.; Patthey, F.; Fernandes, E.; et al. Magnetic remanence in single atoms. *Science* **2016**, *352*, 318–321. https://doi.org/10.1126/science.aad9898.
11. Zadrozny, J.M.; Niklas, J.; Poluektov, O.G.; Freedman, D.E. Millisecond Coherence Time in a Tunable Molecular Electronic Spin Qubit. *ACS Cent. Sci.* **2015**, *1*, 488–492. https://doi.org/10.1021/acscentsci.5b00338.
12. Goodwin, C.A.P.; Ortu, F.; Reta, D.; Chilton, N.F.; Mills, D.P. Molecular magnetic hysteresis at 60 kelvin in dysprosocenium. *Nature* **2017**, *548*, 439–442. https://doi.org/10.1038/nature23447.
13. Bader, K.; Dengler, D.; Lenz, S.; Endeward, B.; Jiang, S.D.; Neugebauer, P.; van Slageren, J. Room temperature quantum coherence in a potential molecular qubit. *Nat. Commun.* **2014**, *5*, 5304. https://doi.org/10.1038/ncomms6304.
14. Guo, F.-S.; Day, B.M.; Chen, Y.-C.; Tong, M.-L.; Mansikkamaki, A.; Layfield, R.A. A Dysprosium Metallocene Single-Molecule Magnet Functioning at the Axial Limit. *Angew. Chem. Int. Ed.* **2017**, *56*, 11445–11449. https://doi.org/10.1002/anie.201705426.
15. Pope, M.T.; Müller, A. Polyoxometalate Chemistry: An Old Field with New Dimensions in Several Disciplines. *Angew. Chem. Int. Ed.* **1991**, *30*, 34–48. https://doi.org/10.1002/anie.199100341.

16. Long, D.L.; Tsunashima, R.; Cronin, L. Polyoxometalates: Building Blocks for Functional Nanoscale Systems. *Angew. Chem. In.t Ed.* **2010,** *49*, 1736–1758. https://doi.org/10.1002/anie.200902483.
17. Krivovichev, S.V. Which inorganic structures are the most complex? *Angew. Chem. Int. Ed.* **2014**, *53*, 654–661. https://doi.org/10.1002/anie.201304374.
18. Wang, S.-S.; Yang, G.-Y. Recent advances in polyoxometalate-catalyzed reactions. *Chem. Rev.* **2015**, *115*, 4893–4962. https://doi.org/10.1021/cr500390v.
19. Song, Y.-F.; Tsunashima, R. Recent advances on polyoxometalate-based molecular and composite materials. *Chem. Soc. Rev.* **2012**, *41*, 7384–7402. https://doi.org/10.1039/c2cs35143a.
20. Ji, Y.; Huang, L.; Hu, J.; Streb, C.; Song, Y.-F. Polyoxometalate-functionalized nanocarbon materials for energy conversion, energy storage and sensor systems. *Energy Environ. Sci.* **2015**, *8*, 776–789. https://doi.org/10.1039/c4ee03749a.
21. Baldoví, J.J.; Rosaleny, L.E.; Ramachandran, V.; Christian, J.; Dalal, N.S.; Clemente-Juan, J.M.; Yang, P.; Kortz, U.; Gaita-Ariño, A.; Coronado, E. Molecular spin qubits based on lanthanide ions encapsulated in cubic polyoxopalladates: Design criteria to enhance quantum coherence. *Inorg. Chem. Front.* **2015**, *2*, 893–897. https://doi.org/10.1039/c5qi00142k.
22. Chen, X.; Zhou, Y.; Roy, V.A.L.; Han, S.T. Evolutionary Metal Oxide Clusters for Novel App.lications: Toward High-Density Data Storage in Nonvolatile Memories. *Adv. Mater.* **2018**, *30*, 1703950. https://doi.org/10.1002/adma.201703950.
23. Clemente-Juan, J.M.; Coronado, E.; Gaita-Arino, A. Magnetic polyoxometalates: From molecular magnetism to molecular spintronics and quantum computing. *Chem. Soc. Rev.* **2012**, *41*, 7464–7478. https://doi.org/10.1039/c2cs35205b.
24. Baldovi, J.J.; Cardona-Serra, S.; Clemente-Juan, J.M.; Coronado, E.; Gaita-Arino, A.; Prima-Garcia, H. Coherent manipulation of spin qubits based on polyoxometalates: The case of the single ion magnet $[GdW_{30}P_5O_{110}]^{14-}$. *Chem. Commun.* **2013**, *49*, 8922–8924. https://doi.org/10.1039/c3cc44838j.
25. Shiddiq, M.; Komijani, D.; Duan, Y.; Gaita-Arino, A.; Coronado, E.; Hill, S. Enhancing coherence in molecular spin qubits via atomic clock transitions. *Nature* **2016**, *531*, 348–351. https://doi.org/10.1038/nature16984.
26. Baldoví, J.J.; Kondinski, A. Exploring High-Symmetry Lanthanide-Functionalized Polyoxopalladates as Building Blocks for Quantum Computing. *Inorganics* **2018,** *6*, 101. https://doi.org/10.3390/inorganics6040101.
27. Monakhov, K.Y.; Bensch, W.; Kogerler, P. Semimetal-functionalised polyoxovanadates. *Chem Soc. Rev.* **2015**, *44*, 8443–8483. https://doi.org/10.1039/c5cs00531k.
28. Kogerler, P.; Tsukerblat, B.; Muller, A. Structure-related frustrated magnetism of nanosized polyoxometalates: Aesthetics and properties in harmony. *Dalton Trans.* **2009**, *39*, 21–36. https://doi.org/10.1039/b910716a.
29. Monakhov, K.Y.; Moors, M.; Kögerler, P. Chapter Nine—Perspectives for Polyoxometalates in Single-Molecule Electronics and Spintronics. In *Adv. Inorg. Chem.* **2017**, *69*, 251–286. https://doi.org/10.1016/bs.adioch.2016.12.009.
30. Kortz, U.; Müller, A.; van Slageren, J.; Schnack, J.; Dalal, N.S.; Dressel, M. Polyoxometalates: Fascinating structures, unique magnetic properties. *Coord. Chem. Rev.* **2009**, *253*, 2315–2327. https://doi.org/10. 1016/j.ccr.2009.01.014.
31. Kondinski, A.; Monakhov, K.Y. Breaking the Gordian Knot in the Structural Chemistry of Polyoxometalates: Copper(II)-Oxo/Hydroxo Clusters. *Chem. A Eur. J.* **2017**, *23*, 7841–7852. https://doi.org/10.1002/chem.201605876.
32. Mal, S.S.; Kortz, U. The wheel-shaped Cu20 tungstophosphate $[Cu_{20}Cl(OH)_{24}(H_2O)_{12}(P_8W_{48}O_{184})]^{25-}$ Ion. *Angew. Chem. Int. Ed.* **2005**, *44*, 3777–3780. https://doi.org/10.1002/anie.200500682.
33. Shi, L.; Li, B.; Wu, L.X. Polyoxometalates as inorganic chiral ligands for the synthesis of chiral nanoparticles. *Chem Commun* **2014**, *51*, 172–175. https://doi.org/10.1039/C4CC07750D.
34. Ritchie, C.; Boskovic, C. Polyoxometalates as Ligands for Functional Lanthanoid Complexes. In *Polyoxometalate Chemistry*; World Scientific: Singapore, 2013; Volume 8, pp. 201–241. https://doi.org/10.1142/9789814458986_0006.
35. Izarova, N.V.; Kögerler, P. Chapter 06—Polyoxometalates-based single molecule magnets. In *Trends in Polyoxometalate Research*; Ruhlmann, L.; Schaming, D., Eds.; Nova Science Publishers: Hapog, NY, USA, 2015; pp. 121–149.
36. Boskovic, C. Rare Earth Polyoxometalates. *Acc. Chem. Res.* **2017**, *50*, 2205–2214. https://doi.org/10.1021/acs.accounts.7b00197.
37. Reinoso, S. Heterometallic 3d-4f polyoxometalates: Still an incipient field. *Dalton Trans.* **2011**, *40*, 6610–6615. https://doi.org/10.1039/c1dt10174a.
38. Klemperer, W.G. Introduction to Early Transition Metal Polyoxoanions. *Inorg. Synth.* **1990**, *27*, 71–85.
39. Kondinski, A.; Parac-Vogt, T.N. Keggin Structure, Quo Vadis? *Front. Chem.* **2018**, *6*. 346. https://doi.org/10.3389/fchem.2018.00346.
40. Chermette, H.; Lefebvre, F. Theoretical study of the four isomers of $[SiW_{11}O_{39}]^{8-}$: Structure, stability and physical properties. *Comptes Rendus Chim.* **2012**, *15*, 143–151. https://doi.org/10.1016/j.crci.2011.09.002.
41. Simms, C.; Kondinski, A.; Parac-Vogt, T.N. Front Cover: Metal-Addenda Substitution in Plenary Polyoxometalates and in their Modular Transition Metal Analogues. *Eur. J. Inorg. Chem.* **2020**, *2020*, 2558–2558. https://doi.org/10.1002/ejic.202000597.
42. Kondinski, A.; Rasmussen, M.; Mangelsen, S.; Pienack, N.; Simjanoski, V.; Näther, C.; Stares, D.L.; Schalley, C.A.; Bensch, W. Composition-driven archetype dynamics in polyoxovanadates. *Chem. Sci.* **2022**, *13*, 6397-6412. https://doi.org/10.1039/D2SC01004F.
43. Busche, C.; Vila-Nadal, L.; Yan, J.; Miras, H.N.; Long, D.L.; Georgiev, V.P.; Asenov, A.; Pedersen, R.H.; Gadegaard, N.; Mirza, M.M.; et al. Design and fabrication of memory devices based on nanoscale polyoxometalate clusters. *Nature* **2014**, *515*, 545–549. https://doi.org/10.1038/nature13951.
44. Bösing, M.; Loose, I.; Pohlmann, H.; Krebs, B. New Strategies for the Generation of Large Heteropolymetalate Clusters: The β-B-SbW_9 Fragment as a Multifunctional Unit. *Chem. Eur. J.* **1997**, *3*, 1232–1237. https://doi.org/10.1002/chem.19970030810.

45. Kim, K.C.; Gaunt, A.; Pope, M.T. New heteropolytungstates incorporating dioxouranium(VI). Derivatives of a-[SiW_9O_{34}]$^{10-}$, a-[AsW_9O_{33}]$^{9-}$, g-[$SiW_{10}O_{36}$]$^{8-}$, and [$As_4W_{40}O_{140}$]$^{28-}$. *J. Cluster Sci.* **2002**, *13*, 423–436. https://doi.org/10.1023/A:1020507201056.
46. Loose, I.; Droste, E.; Bösing, M.; Pohlmann, H.; Dickman, M.H.; Rosu, C.; Pope, M.T.; Krebs, B. Heteropolymetalate Clusters of the Subvalent Main Group Elements Bi^{III} and Sb^{III} *Inorg. Chem.* **1999**, *38*, 2688–2694. https://doi.org/10.1021/ic981313m.
47. Hussain, F.; Patzke, G.R. Self-assembly of dilacunary building blocks into high-nuclear [$Ln_{16}As_{16}W_{164}O_{576}(OH)_8(H_2O)_{42}$]$^{80-}$ (Ln = Eu^{III}, Gd^{III}, Tb^{III}, Dy^{III}, and Ho^{III}) polyoxotungstates. *CrystEngComm* **2011**, *13*, 530–536. https://doi.org/10.1039/C003489D.
48. Robert, F.; Leyrie, M.; Herve, G. Structure of potassium diaquatricuprooctadecatungstodiarsenate(III)(12-) undecahydrate. *Acta Crystallogr. Sect. B* **1982**, *38*, 358–362. https://doi.org/10.1107/S0567740882002970.
49. Pope, M.T.; Wei, X.; Wassermann, K.; Dickman, M.H. New developments in the chemistry of heteropolytungstates of rhodium and cerium. *Chemistry* **1998**, *1*, 297–304. https://doi.org/10.1016/S1387-1609(98)80168-0.
50. Dolbecq, A.; Dumas, E.; Mayer, C.R.; Mialane, P. Hybrid Organic−Inorganic Polyoxometalate Compounds: From Structural Diversity to Applications. *Chem. Rev.* **2010**, *110*, 6009–6048. https://doi.org/10.1021/cr1000578.
51. Weakley, T.J.R.; Evans, H.T.; Showell, J.S.; Tourné, G.F.; Tourné, C.M. 18-Tungstotetracobalto(II)diphosphate and related anions: A novel structural class of heteropolyanions. *J. Chem. Soc. Chem. Comm.* **1973**, 139–140. https://doi.org/10.1039/c39730000139.
52. Knoth, W.H.; Domaille, P.J.; Farlee, R.D. Anions of the type ($RMOH_2)_3W_{18}P_2O_{68}^{9-}$ and [$H_2OCo]_3W_{18}P_2O_{68}^{12-}$. A reinvestigation of "B,b-$W_9PO_{34}^{9-}$". *Organometallics* **1985**, *4*, 62–68. https://doi.org/10.1021/om00120a012.
53. Robert, F.; Leyrie, M.; Herve, G.; Teze, A.; Jeannin, Y. Crystal structure of ammonium dicobalto(II)-40-tungstotetraarsenate(III). Allosteric effects in the ligand. *Inorg. Chem.* **1980**, *19*, 1746–1752. https://doi.org/10.1021/ic50208a065.
54. Kortz, U.; Savelieff, M.G.; Bassil, B.S.; Dickman, M.H. A large, novel polyoxotungstate: [$As^{III6}W_{65}O_{217}(H_2O)_7$]$^{26-}$. *Angew. Chem. Int. Ed.* **2001,** *40*, 3384–3386. https://doi.org/10.1002/1521-3773(20010917)40:18<3384::AID-ANIE3384>3.0.CO;2-O.
55. Hervé, G.; Tézé, A.; Contant, R. General Principles of The Synthesis of Polyoxometalates in Aqueous Solution. In *Polyoxometalate Molecular Science*; Borrás-Almenar, J.J., Coronado, E., Müller, A., Pope, M., Eds.; Springer: Dordrecht, The Netherlands, 2003; pp. 33–54. https://doi.org/10.1007/978-94-010-0091-8_2.
56. Hussain, F.; Conrad, F.; Patzke, G.R. A Gadolinium-Bridged Polytungstoarsenate(III) Nanocluster: [$Gd_8As_{12}W_{124}O_{432}(H_2O)_{22}$]$^{60-}$. *Angew. Chem. Int. Ed.* **2009**, *48*, 9088–9091. https://doi.org/10.1002/anie.200903299.
57. Limanski, E.M.; Drewes, D.; Droste E.; Böhner, R.; Krebs, B. Syntheses and X-ray characterisation of novel tellurium-substituted lacunary polyoxotungstates containing V^{IV}, Co^{II}, Ni^{II} and Zn^{II} as heteroatoms. *J. Mol. Struct.* **2003**, *656*, 17–25. https://doi.org/10.1016/S0022-2860(03)00340-5.
58. Kortz, U.; Al-Kassem, N.K.; Savelieff, M.G.; Al Kadi, N.A.; Sadakane, M. Synthesis and Characterization of Copp.er-, Zinc-, Manganese-, and Cobalt-Substituted Dimeric Heteropolyanions, [(α-$XW_9O_{33})_2M_3(H_2O)_3$]$^{n-}$ (n = 12, X = As^{III}, Sb^{III}, M = Cu^{2+}, Zn^{2+}; n = 10, X = Se^{IV}, Te^{IV}, M = Cu^{2+}) and [(α-$AsW_9O_{33})_2WO(H_2O)M_2(H_2O)_2$]$^{10-}$ (M = Zn^{2+}, Mn^{2+}, Co^{2+}). *Inorg. Chem.* **2001**, *40*, 4742–4749. https://doi.org/10.1021/ic0101477.
59. Saini, M.K.; Gupta, R.; Singh, S.; Hussain, F. Synthesis, crystal structure and catalytic activity of the guanidinium cation directed nickel(II)-containing open Wells–Dawson 19-tungstodiarsenate(III) [{$Ni(H_2O)_4$}$_2${$Na(H_2O)$}$As_2W_{19}O_{67}(H_2O)$]$^{9-}$. *RSC Adv.* **2015**, *5*, 25273–25278. https://doi.org/10.1039/C5RA01426C.
60. Kokoszka, G.F.; Padula, F.; Goldstein, A.S.; Venturini, E.L.; Azevedo, L.; Siedle, A.R. Magnetic interactions in a copp.er(II) trimer encapsulated in a molecular metal oxide cluster. *Inorg. Chem.* **1988**, *27*, 59–62. https://doi.org/10.1021/ic00274a014.
61. Stowe, C.A.; Nellutla, S.; Dalal, S.N.; Kortz, U. Magnetic Properties of Lone-Pair-Containing, Sandwich-Type Polyoxoanions: A Detailed Study of the Heteroatomic Effect. *Eur. J. Inorg. Chem.* **2004**, *2004*, 3792–3797. https://doi.org/10.1002/ejic.200400234.
62. Choi, K.Y.; Matsuda, Y.H.; Nojiri, H.; Kortz, U.; Hussain, F.; Dalal, N.S. Half-Step magnetization in the polyoxometalate family with {Cu_3}-type triangular spin ring. *J. Phys. Conf. Ser.* **2006**, *51*, 95–98. https://doi.org/10.1088/1742–6596/51/1/020.
63. Ma, X.; Su, Z.; Zhao, Z.; Zhou, B.; Yu, K.; Shang, Y.; Wang, M.; Tian, Y. Synthesis, crystal structure and properties of a 2D hexa-nuclear ring Cu/Na-substituted sandwich-type arsenotungstate. *Inorg. Chem. Commun.* **2019**, *103*, 136-141. https://doi.org/10.1016/j.inoche.2019.03.021.
64. Zhang, Z.; Yang, L.; Xu, N.; Li X.-H. A New Multi-Copper-Substituted Tetramer Tungstoantimonate: Synthesis, Photocatalytic and Electrochemical Properties. *J. Clust. Sci.* **2022**, *33*, 1249–1255 . https://doi.org/10.1007/s10876-021-02059-8.
65. Mialane, P.; Marrot, J.; Rivière, E.; Nebout, J.; Hervé, G. Structural Characterization and Magnetic Properties of Sandwich-Type Tungstoarsenate Complexes. Study of a Mixed-Valent V^{IV}_2/V^V Heteropolyanion. *Inorg. Chem.* **2001**, *40*, 44–48. https://doi.org/10.1021/ic000641v.
66. Chai, F.; Chen, Y.; Yang, Z.; Su, L.; Sun, Y. Synthesis and characterization of a new Hervé-type tungstoantimonite based on α-[SbW_9O_{33}]$^{9-}$ unit. *J. Mol. Struct.* **2013**, *1051*, 101–106. https://doi.org/10.1016/j.molstruc.2013.07.050.
67. Choi, K.-Y.; Dalal, N.S.; Reyes, A.P.; Kuhns, P.L.; Matsuda, Y.H.; Nojiri, H.; Mal, S.S.; Kortz, U. Pulsed-field magnetization, electron spin resonance, and nuclear spin-lattice relaxation in the {Cu_3} spin triangle. *Phys. Rev. B* **2008**, *77*, 24406–24406. https://link.aps.org/doi/10.1103/PhysRevB.77.024406.
68. Oms, O.; Yang, S.; Salomon, W.; Marrot, J.; Dolbecq, A.; Rivière, E.; Bonnefont, A.; Ruhlmann, L.; Mialane, P. Heteroanionic Materials Based on Copper Clusters, Bisphosphonates, and Polyoxometalates: Magnetic Properties and Comparative Electrocatalytic NO_x Reduction Studies. *Inorg. Chem.* **2016**, *55*, 1551–1561. https://doi.org/10.1021/acs.inorgchem.5b02456.
69. David, L.; Crăciun, C.; Chis, V.; Tetean, R. EPR and HF-EPR study of a trinuclear Mn^{II} cluster encapsulated in one sandwich-type heteropolyanion. *Solid State Commun.* **2002**, *121*, 675–678. https://doi.org/10.1016/S0038-1098(02)00068-6.

70. Von Allmen, K.D.; Grundmann, H.; Linden, A.; Patzke, G.R. Synthesis and Characterization of 0D–3D Copp.er-Containing Tungstobismuthates Obtained from the Lacunary Precursor $Na_9[B\text{-}\alpha\text{-}BiW_9O_{33}]$. *Inorg. Chem.* **2017**, *56*, 327–335. https://doi.org/10.1021/acs.inorgchem.6b02217.
71. Rusu, D.; Tomsa, A.R.; Turdean, G.L.; Cojocaru, I.; Baban, O.; Rusu, M. Synthesis and investigation of the copp.er(II)-substituted polyoxotungstate based on α-B-$[BiW_9O_{33}]^{9-}$ *Rev. Roum. de Chim.* **2012**, *57*, 327–336.
72. Yamase, T.; Botar, B.; Ishikawa, E.; Fukaya, K. Chemical Structure and Intramolecular Spin-Exchange Interaction of $[(VO)_3(SbW_9O_{33})_2]^{12-}$. *Chem. Lett.* **2001**, *30*, 56–57. https://doi.org/10.1246/cl.2001.56.
73. Yamase, T.; Ishikawa, E.; Fukaya, K.; Nojiri, H.; Taniguchi, T.; Atake, T. Spin-Frustrated (VO)36+-Triangle-Sandwiching Octadecatungstates as a New Class of Molecular Magnets. *Inorg. Chem.* **2004**, *43*, 8150–8157. https://doi.org/10.1021/ic049669n.
74. Kohama, Y.; Kawaji, H.; Atake, T.; Fukaya, K.; Yamase, T. Low-temperature heat capacity of triangle antiferromagnetic molecular clusters $K_{12}[(VO)_3(SbW_9O_{33})_2]\cdot 15H_2O$ and $K_{12}[(VO)_3(BiW_9O_{33})_2]\cdot 29H_2O$. *J. Solid State Chem.* **2009**, *182*, 1468–1472. https://doi.org/10.1016/j.jssc.2009.03.018.
75. Liu, X.-M.; Wang, C.-R.; Liu, B.; Xue, G.-L.; Hu, H.-M.; Wang, J.-W.; Fu, F. Structure and Magnetic Properties of Pyridine Coordinated Sandwich-type Heteropolyanion $\{[Na(H_2O)_2]_3[Ni(C_5H_5N)]_3(AsW_9O_{33})_2\}^{9-}$. *Chin. J. Chem.* **2005**, *23*, 1412–1416. https://doi.org/10.1002/cjoc.200591412.
76. Wu, L.; Liu, B.; Dong, X.; Yu, C.; Yan, Y.; Hu, H.; Xue, G. A sandwich-type tungstoantimonate containing trinuclear nickel ions modified with aminopyrazine ligand. *Inorg. Chem. Commun.* **2015**, *56*, 13–16. https://doi.org/10.1016/j.inoche.2015.03.041.
77. Liu, J.-M.; Wang, L.; Yu, K.; Su, Z.-H.; Wang, C.-X.; Wang, C.-M.; Zhou, B.-B. Synthesis, crystal structure and properties of sandwich type compounds based on $\{AsW_9\}$ and a hexa-nuclear unit with three supp.orting TM–triazole complexes. *New J. Chem.* **2015**, *39*, 1139–1147. https://doi.org/10.1039/C4NJ01138D.
78. Cui, R.-R.; Wang, H.-L.; Yang, X.-Y.; Ren, S.-H.; Hu, H.-M.; Fu, F.; Wang, J.-W.; Xue, G.-L. Imidazole Coordinated Sandwich-type Antimony Poly-oxotungstates $Na_9[\{Na(H_2O)_2\}_3\{M(C_3H_4N_2)\}_3(SbW_9O_{33})_2]\cdot xH_2O$ ($M=Ni^{II}$, Co^{II}, Zn^{II}, Mn^{II}). *Chin. J. Chem.* **2007**, *25*, 176–181. https://doi.org/10.1002/cjoc.200790036.
79. Han, L.; Zhang, P.-P.; Liu, H.-S.; Pang, H.-J.; Chen, Y.; Peng, J. Functionalized Sandwich-Type Polyoxometalates Based on the Polynuclear Manganese Cluster and Imidazole Ligands. *J. Cluster Sci.* **2010**, *21*, 81–91. https://doi.org/10.1007/s10876-010-0322-x.
80. Chai, D.-F.; Ma, Z.; Yan, H.; Qiu, Y.; Liu, H.; Guo, H.-D.; Gao, G.-G. Synergistic effect of sandwich polyoxometalates and copp.er–imidazole complexes for enhancing the peroxidase-like activity. *RSC Adv.* **2015**, *5*, 78771–78779. https://doi.org/10.1039/C5RA13265G.
81. Liu, H.; Qin, C.; Wei, Y.-G.; Xu, L.; Gao, G.-G.; Li, F.-Y.; Qu, X.-S. Copp.er-Complex-Linked Polytungsto-Bismuthate (-Antimonite) Chain Containing Sandwich Cu(II) Ions Partially Modified with Imidazole Ligand. *Inorg. Chem.* **2008**, *47*, 4166–4172. https://doi.org/10.1021/ic7022264.
82. Sun, M.; Wang, T.; Li, F.; Sun, Z.; Xu, L. A novel sandwich-tungstoantimonate cluster with Fe^{II} ions: Synthesis, magnetic property and electrochemical sensing of dopamine. *New J. Chem.* **2018**, *42*, 7480–7484. https://doi.org/10.1039/C8NJ00187A.
83. Liu, H.; Liu, Y.; Liu, H.; Shi, C.; Liu, F.; Liu, H. Trinuclear cobalt(II) sandwiched polyoxotungstobismuthate with antennal copp.er(II)-complex: A new method to combine hetero–transition–metallic ions. *Inorg. Chem. Commun.* **2009**, *12*, 1–3. https://doi.org/10.1016/j.inoche.2008.10.009.
84. Chen, B.; Chen, W.; Liu, W.; Li, Y.; Wang, X.; Wang, E. Two new methylimidazole modified Hervé-sandwich-type polytungstoantimonates. *J. Coord. Chem.* **2011**, *64*, 71–81. https://doi.org/10.1080/00958972.2010.527003..
85. Liu, H.; Xu, L.; Gao, G.; Li, F.; Jiang, N. Sandwich transitional metal complexes with tungstobismuthates and 1-methylimidazole ligands: Syntheses, structures and magnetic properties. *J. Mol. Struct.* **2008**, *878*, 124–130. https://doi.org/10.1016/j.molstruc.2007.08.015.
86. Wu, Q.; Ju, H.; Tao, J.; Chen, Z.; Li, J.; Wang, F.; Cai, Q.; Sun, L.; Pan, X. New Member of Organic Ligand Functionalized TMSP: Synthesis, Characterized and Properties of $Na_{15}[(Mn^{II}(COOH))_3(AsW_9O_{33})_2]\cdot 15H_2O$. *J. Cluster Sci.* **2015**, *26*, 1811–1820. https://doi.org/10.1007/s10876-015-0880-z.
87. Liu, Y.; Cao, J.; Wang, Y.; Li, Y.; Zhao, J.; Chen, L.; Ma, P.; Niu, J. Hydrothermal synthesis and structural characterization of an organic–inorganic hybrid sandwich-type tungstoantimonate $[Cu(en)_2(H_2O)]_4[Cu(en)_2(H_2O)_2][Cu_2Na_4(\alpha\text{-}SbW_9O_{33})_2]\cdot 6H_2O$. *J. Solid State Chem.* **2014**, *209*, 113–119. https://doi.org/10.1016/j.jssc.2013.10.033.
88. Ma, P.; Zhang, Y.; Li, J. Two new 2-D frameworks based on tetra-copp.er(II)-substituted sandwich-type polyoxotungstate anions and $[Cu_2(dien)_2(OH)]^{3+}$ cations. *J. Coord. Chem.* **2014**, *67*, 2238–2248. https://doi.org/10.1080/00958972.2014.940336.
89. Kortz, U.; Nellutla, S.; Stowe, A.C.; Dalal, N.S.; van Tol, J.; Bassil, B.S. Structure and Magnetism of the Tetra-Copp.er(II)-Substituted Heteropolyanion $[Cu_4K_2(H_2O)_8(\alpha\text{-}AsW_9O_{33})_2]^{8-}$. *Inorg. Chem.* **2004**, *43*, 144–154. https://doi.org/10.1021/ic034697b.
90. Gupta, R.; Khan, I.; Hussain, F.; Bossoh, A.M.; Mbomekallé, I.M.; de Oliveira, P.; Sadakane, M.; Kato, C.; Ichihashi, K.; Inoue, K.; et al. Two New Sandwich-Type Manganese $\{Mn_5\}$-Substituted Polyoxotungstates: Syntheses, Crystal Structures, Electrochemistry, and Magnetic Properties. *Inorg. Chem.* **2017**, *56*, 8759–8767. https://doi.org/10.1021/acs.inorgchem.6b02994.
91. Zhao, H.; Tao, L.; Zhang, F.; Zhang, Y.; Liu, Y.; Xu, H.; Diao, G.; Ni, L. Transition metal substituted sandwich-type polyoxometalates with a strong metal–C (imidazole) bond as anticancer agents. *Chem Commun* **2018**, *55*, 1096–1099. https://doi.org/10.1039/c8cc07884j.
92. Hua, J.; Ma, X.; Ma, P.; Wang, J.; Niu, J. Crystal Structure and Magnetic Property of a 2-D Hexa-Circular Ring Cu(II)/Na(I)-Substituted Sandwich-Type Arsenotungstate. *J. Clus. Sci.* **2013**, *24*, 689–700. https://doi.org/10.1007/s10876-012-0536-1.
93. Yamase, T.; Fukaya, K.; Nojiri, H.; Ohshima, Y. Ferromagnetic Exchange Interactions for Cu_6^{12+} and Mn_6^{12+} Hexagons Sandwiched by Two B-α-$[XW_9O_{33}]^{9-}$ (X = As^{III} and Sb^{III}) Ligands in D3d-Symmetric Polyoxotungstates. *Inorg. Chem.* **2006**, *45*, 7698–7704. https://doi.org/10.1002/chin.200650027.

94. Yamase, T.; Ishikawa, H.; Abe, H.; Fukaya, K.; Nojiri, H.; Takeuchi, H. Molecular Magnetism of M_6 Hexagon Ring in D_{3d} Symmetric $[(MCl)_6(XW_9O_{33})_2]^{12-}$ (M = Cu^{II} and Mn^{II}, X = Sb^{III} and As^{III}). *Inorg. Chem.* **2012**, *51*, 4606–4619. https://doi.org/10.1021/ic202513q.
95. Oshima, Y.; Nojiri, H.; Fukaya, K.; Yamase, T. Magnetic properties of the ferromagnetic ring-shaped single-molecule magnet Cu_6. *J. Phys. Conf. Ser.* **2006**, *51*, 195–198. https://doi.org/10.1088/1742-6596/51/1/045.
96. Zamstein, N.; Tarantul, A.A.; Tsukerblat, B. Magnetic Excitations in Cu6 and Mn6 Hexagons Embedded in D_{3d}-Symmetric Polyoxotungstates. *Inorg. Chem.* **2007**, *46*, 8851–8858. https://doi.org/10.1021/ic700585c.
97. Zhao, Z.; Zhou, B.; Zheng, S.; Su, Z.; Wang, C. Hydrothermal synthesis, crystal structure and magnetic characterization of three hexa-M substituted tungstoarsenates (M = Ni, Zn and Mn). *Inorg. Chim. Acta* **2009**, *362*, 5038–5042. https://doi.org/10.1016/j.ica.2009.08.015.
98. Liu, J.; Luo, J.; Han, Q.; Cao, J.; Chen, L.; Song, Y.; Zhao, J. Coexistence of long-range ferromagnetic ordering and spin-glass behavior observed in the first inorganic–organic hybrid 1-D oxalate-bridging nona-MnII sandwiched tungstoantimonate chain. *J. Mater. Chem. C* **2017**, *5*, 2043–2055. https://doi.org/10.1039/C6TC05479J.
99. Merca, A.; Müller, A.; van Slageren, J.; Läge, M.; Krebs, B. Systematic Study of the Interaction Between V^{IV} Centers and Lanthanide Ions M^{III} in Well Defined $\{V^{IV}{}_2M^{III}\}\{As^{III}W_9O_{33}\}_2$ Sandwich Type Clusters: Part 1. *J. Cluster Sci.* **2007**, *18*, 711–719. https://doi.org/10.1007/s10876-007-0144-7.
100. Merca, A.; Schnack, J.; van Slageren, J.; Glaser, T.; Bögge, H.; Hoeke, V.; Läge, M.; Müller, A.; Krebs, B. Systematic Study of the Interaction Between V^{IV} Centers and Ln^{III} Ions in Well Defined $\{V_2{}^{IV}Ln^{III}\}\{As^{III}W_9O_{33}\}_2$ Sandwich-Type Clusters: Part 2. *J. Clust. Sci.* **2013**, *24*, 979–988. https://doi.org/10.1007/s10876-013-0588-x.
101. Wang, K.-Y.; Bassil, B.S.; Xing, X.; Keita, B.; Bindra, J.K.; Diefenbach, K.; Dalal, N.S.; Kortz, U. Incorporation of Transition-Metal-Ion Guests (Co^{2+}, Ni^{2+}, Cu^{2+}, Zn^{2+}) into the Ti_2-Containing 18-Tungsto-2-arsenate(III) Monolacunary Host. *Eur. J. Inorg. Chem.* **2016**, *2016*, 5519–5529. https://doi.org/10.1002/ejic.201601354.
102. Wang, K.-Y.; Lin, Z.; Bassil, B.S.; Xing, X.; Haider, A.; Keita, B.; Zhang, G.; Silvestru, C.; Kortz, U. Ti_2-Containing 18-Tungsto-2-Arsenate(III) Monolacunary Host and the Incorporation of a Phenylantimony(III) Guest. *Inorg. Chem.* **2015**, *54*, 10530–10532. https://doi.org/10.1021/acs.inorgchem.5b01863.
103. Chen, L.; Jin, M.; Zheng, R.; Liu, Y.; Zhao, J. Two 1,3-bis[tris(hydroxymethyl)methylamino]propane functionalized 3d–4f heterometallic arsenotungstates. *Inorg. Chem. Commun.* **2019**, *105*, 63–68. https://doi.org/10.1016/j.inoche.2019.04.025.
104. Dolbecq, A.; Compain, J.-D.; Mialane, P.; Marrot, J.; Rivière, E.; Sécheresse, F. Water Substitution on Iron Centers: From 0D to 1D Sandwich Type Polyoxotungstates. *Inorg. Chem.* **2008**, *47*, 3371–3378. https://doi.org/10.1021/ic7024186.
105. Rusu, D.; Roşu, C.; Crăciun, C.; David, L.; Rusu, M.; Marcu, G. FT-IR, UV–VIS and EPR investigations of multicopp.er polyoxotungstates with Bi^{III} as heteroatom. *J. Mol. Struct.* **2001,** *563–564*, 427–433. https://doi.org/10.1016/S0022-2860(00)00828-0.
106. Sun, M.; Li, F.; Yu, L.; Wang, Y.; Xu, L. Synthesis of $[Sb_2W_{20}Fe^{II}{}_2(H_2O)_6O_{70}]^{10-}$ with iron powder under mild conditions and its app.lications in both catalytic Fenton reaction and electrochemical sensing of ascorbic acid. *Dalton Trans.* **2016**, *45*, 2417–2421. https://doi.org/10.1039/C5DT04637H.
107. Kortz, U.; Savelieff, M.G.; Bassil, B.S.; Keita, B.; Nadjo, L. Synthesis and Characterization of Iron(III)-Substituted, Dimeric Polyoxotungstates, $[Fe_4(H_2O)_{10}(\beta\text{-}XW_9O_{33})_2]^{n-}$ (n = 6, X = As^{III}, Sb^{III}; n = 4, X = Se^{IV}, Te^{IV}). *Inorg. Chem.* **2002**, *41*, 783–789. https://doi.org/10.1021/ic010855s.
108. Carraro, M.; Bassil, B.S.; Sorarù, A.; Berardi, S.; Suchopar, A.; Kortz, U.; Bonchio, M. A Lewis acid catalytic core sandwiched by inorganic polyoxoanion caps: Selective H_2O_2-based oxidations with $[Al^{III}4(H_2O)_{10}(\beta\text{-}XW_9O_{33}H)_2]^{6-}$ (X = As^{III}, Sb^{III}). *Chem. Commun.* **2013**, *49*, 7914–7916. https://doi.org/10.1039/c3cc44077j.
109. Sartorel, A.; Carraro, M.; Scorrano, G.; Bassil, B.S.; Dickman, M.H.; Keita, B.; Nadjo, L.; Kortz, U.; Bonchio, M. Iron-Substituted Polyoxotungstates as Inorganic Synzymes: Evidence for a Biomimetic Pathway in the Catalytic Oxygenation of Catechols. *Chem. Eur. J.* **2009**, *15*, 7854–7858. https://doi.org/10.1002/chem.200901392.
110. Prinz, M.; Takács, A.F.; Schnack, J.; Balasz, I.; Burzo, E.; Kortz, U.; Kuepp.er, K.; Neumann, M. Magnetic and electronic properties of the iron-containing polyoxotungstate $[Fe_4(H_2O)_{10}(\beta\text{-}SbW_9O_{33})_2]^{6-}$. *J. Appl. Phys.* **2006**, *99*, 08J505. https://doi.org/10.1063/1.2173613.
111. Jia, J.; Zhang, Y.; Zhang, P.; Ma, P.; Zhang, D.; Wang, J.; Niu, J. Synthesis and characterization of a series of novel polyoxometalate-supp.orted carbonyl manganese derivatives. *RSC Adv.* **2016**, *6*, 108335–108342. https://doi.org/10.1039/C6RA23547F.
112. Wang, J.-P.; Ma, P.-T.; Li, J.; Niu, H.-Y.; Niu, J.-Y. Self-Assembly of $[B\text{-}SbW_9O_{33}]^{9-}$ Subunit with Transition Metal Ions (Mn^{2+}, Cu^{2+}, Co^{2+}) in Aqueous Solution: Syntheses, Structures and Magnetic Properties of Sandwich Type Polyoxometalates with Subvalent SbIII Heteroatom. *Chem. Asian J.* **2008**, *3*, 822–833. https://doi.org/10.1002/asia.200700363.
113. Zhang, L.; Zhang, Y.; Hao, Z.; Luo, F. Synthesis, Structure, and Magnetic Properties of Three Novel Sandwich-type Tungstobismuthates with Triethanolamine. *J. Inorg. Gen. Chem.* **2010**, *636*, 1991–1997. https://doi.org/10.1002/zaac.201000011.
114. Bi, L.-H.; Hou, G.-F.; Bao, Y.-Y.; Li, B.; Wu, L.-X.; Gao, Z.-M.; McCormac, T.; Mal, S.S.; Dickman, M.H.; Kortz, U. Syntheses and Crystal Structures of dmso-Coordinated Tungstoantimonates(III) and -bismuthates(III). *Eur. J. Inorg. Chem.* **2009**, *2009*, 5259–5266. https://doi.org/10.1002/ejic.200900590.
115. Lu, C.; Chen, Y.; Li, H.; Chen, L.; Zhai, C.; Zhao, J. An organic–inorganic hybrid tetra-FeIII incorporated Krebs-sandwich-type tungstoantimonate decorated by pyridine carboxylic ligand. *Inorg. Chem. Commun.* **2018**, *91*, 85–90. https://doi.org/10.1016/j.inoche.2018.03.001.

116. Artetxe, B.; Reinoso, S.; Felices, L.S.; Vitoria, P.; Pache, A.; Martín-Caballero, J.; Gutiérrez-Zorrilla, J.M. Functionalization of Krebs-Type Polyoxometalates with N,O-Chelating Ligands: A Systematic Study. *Inorg. Chem.* **2014**, *54*, 241–252. https://doi.org/10.1021/ic502232v.
117. Artetxe, B.; Reinoso, S.; Felices, L.S.; Lezama, L.; Pache, A.; Vicent, C.; Gutiérrez-Zorrilla, J.M. Rearrangement of a Krebs-Type Polyoxometalate upon Coordination of N,O-Bis(bidentate) Ligands. *Inorg. Chem.* **2015**, *54*, 409–411. https://doi.org/10.1021/ic5026729.
118. Niu, J.-Q.; Zhao, Q.; Xin, X.; Zhang, Y.-Q.; Hu, N.; Ma, Y.-Y.; Han, Z.-G. Krebs-type polyoxometalate-based crystalline materials: Synthesis, characterization and catalytic performance. *J. Co-ord. Chem.* **2020**, *73*, 2391–2401. https://doi.org/10.1080/00958972.2020.1802650.
119. Wang, H.-D.; Wang, X.-F.; Su, F.; Li, J.-S.; Zhang, L.-C.; Sang, X.-J.; Zhu, Z.-M. Carboxyethyltin and transition metal co-functionalized tungstoantimonates composited with polypyrrole for enhanced electrocatalytic methanol oxidation. *Dalton Trans.* **2019**, *48*, 2977–2987. https://doi.org/10.1039/c8dt05118f.
120. Das, V.; Kaushik, R.; Hussain, F. Heterometallic 3d-4f polyoxometalates: An emerging field with structural diversity to multiple app.lications. *Coordin. Chem. Rev.* **2020**, *413*, 213271. https://doi.org/10.1016/j.ccr.2020.213271.
121. Chen, Y.; Sun, L.; Chang, S.; Chen, L.; Zhao, J. Synergistic Effect between Different Coordination Geometries of Lanthanides and Various Coordination Modes of 2-Picolinic Acid Ligands Tuning Three Types of Rare 3d–4f Heterometallic Tungstoantimonates. *Inorg. Chem.* **2018**, *57*, 15079–15092. https://doi.org/10.1021/acs.inorgchem.8b02103.
122. Zhao, J.-W.; Cao, J.; Li, Y.-Z.; Zhang, J.; Chen, L.-J. First Tungstoantimonate-Based Transition-Metal–Lanthanide Heterometallic Hybrids Functionalized by Amino Acid Ligands. *Cryst. Growth Des.* **2014**, *14*, 6217–6229. https://doi.org/10.1021/cg5007988.
123. Kondinski, A. Metal–metal bonds in polyoxometalate chemistry. *Nanoscale* **2021**, *13*, 13574–13592. https://doi.org/10.17863/cam.74516.
124. Kondinski, A.; Ghorbani-Asl, M. Polyoxoplatinates as covalently dynamic electron sponges and molecular electronics materials. *Nanoscale Adv.* **2021**, *3*, 5663–5675. https://doi.org/10.1039/d1na00387a.
125. Yi, X.; Izarova, N.V.; Stuckart, M.; Guérin, D.; Thomas, L.; Lenfant, S.; Vuillaume, D.; van Leusen, J.; Duchoň, T.; Nemšák, S.; et al. Probing Frontier Orbital Energies of $\{Co_9(P_2W_{15})_3\}$ Polyoxometalate Clusters at Molecule–Metal and Molecule–Water Interfaces. *J. Am. Chem. Soc.* **2017**, *139*, 14501–14510. https://doi.org/10.1021/jacs.7b07034.
126. Lapham, P.; Vilà-Nadal, L.; Cronin, L.; Georgiev, V.P. Influence of the Contact Geometry and Counterions on the Current Flow and Charge Transfer in Polyoxometalate Molecular Junctions: A Density Functional Theory Study. *J. Phys. Chem. C* **2021**, *125*, 3599–3610. https://doi.org/10.1021/acs.jpcc.0c11038.
127. Charron, G.; Giusti, A.; Mazerat, S.; Mialane, P.; Gloter, A.; Miserque, F.; Keita, B.; Nadjo, L.; Filoramo, A.; Rivière, E.; et al. Assembly of a magnetic polyoxometalate on SWNTs. *Nanoscale* **2009**, *2*, 139–144. https://doi.org/10.1039/b9nr00190e.
128. Kondinski, A.; Menon, A.; Nurkowski, D.; Farazi, F.; Mosbach, S.; Akroyd, J.; Kraft, M. Automated Rational Design of Metal–Organic Polyhedra. *J. Am. Chem. Soc.* **2022**. https://doi.org/10.1021/jacs.2c03402.
129. Kondinski, A. Computational modelling of isomeric polyoxometalates. In *Chemical Modeling*; The Royal Society of Chemistry: Cambrige, UK, 2021; Volume 16, pp. 39–71. https://doi.org/10.1039/9781839162657-00039.